Materials & Design 224 (2022) 111383

Contents lists available at ScienceDirect

Materials & Design

journal homepage: www.elsevier.com/locate/matdes

Modeling fatigue of pre-corroded body-centered cubic metals with unified mechanics theory

Hsiao Wei Lee [a], Hamidreza Fakhri [b], Ravi Ranade [a], Cemal Basaran [a,*], Halina Egner [c], Adam Lipski [d], Michał Piotrowski [d], Stanisław Mroziński [d]

[a] Civil, Structural, and Environ. Engineering, University at Buffalo, NY, USA
[b] McMahon & Mann Consulting Engineering and Geology, P.C, Buffalo, NY, USA
[c] Faculty of Mechanical Engineering, Cracow University of Technology, Kraków, Poland
[d] Faculty of Mechanical Engineering, Bydgoszcz University of Science and Technology, Poland

HIGHLIGHTS

- The ultrasonic vibration fatigue life of pre-corroded ferrite-pearlite low carbon structural steel is modeled with Unified mechanics theory.
- The entropy generation equation for metal under corrosion and ultrasonic vibration are derived analytically.
- An electrochemical cell is built for the corrosion test. Corrosion measurement such as Tafel test and Cyclic polarization test are performed and discussed.
- A fractographic study is performed on the fracture surface of corroded samples and uncorroded reference samples after fatigue tests.
- Simulated corrosion fatigue SN curve based on Unified mechanics theory is compared with the test SN data.

GRAPHICAL ABSTRACT

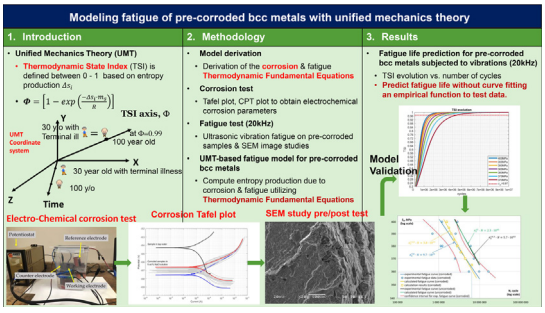

ARTICLE INFO

Article history:
Received 26 October 2022
Revised 11 November 2022
Accepted 15 November 2022
Available online 22 November 2022

Keywords:
Entropy
Unified mechanics theory
Thermodynamics
Corrosion
Fatigue
Vibration
Electrochemistry
Structural steel

ABSTRACT

Corrosion is a common degradation problem in engineering structures. The unified mechanics theory (UMT) was used to develop a model to predict the fatigue life of pre-corroded steel samples with BCC structure. The model was also verified experimentally. For this purpose, A656-grade steel samples were immersed in a 5 wt% sodium chloride (NaCl) solution at a pH of 7. Electrochemical measurements were made with a potentiostat to monitor corrosion. Then, a series of ultrasonic vibration fatigue tests were conducted on these corroded samples at 20 kHz. UMT is ab-initio unification of the laws of Newton and the 2nd law of thermodynamics. Hence no empirical degradation/dissipation function is needed. However, the thermodynamic fundamental equation for metal corrosion and ultrasonic vibration must be analytically derived. The thermodynamic fundamental equation formulates all the entropy generation mechanisms during the corrosion and then during ultrasonic vibrations. The cumulative entropy generation was then used to calculate the Thermodynamic State Index (TSI), which starts at zero and asymptotically approaches one at failure. Hence, TSI predicts the life span. The proposed model results agree well with the experimental results, thus proving that the UMT-based model can predict the high cycle fatigue life of previously corroded samples accurately.

* Corresponding author.
E-mail address: cjb@buffalo.edu (C. Basaran).

https://doi.org/10.1016/j.matdes.2022.111383
0264-1275/

Nomenclature

$\underset{\sim}{A}_j$	Chemical affinity
$\underset{\sim}{A}$	Electrochemical affinity
A_M	Electrochemical affinity for oxidation
A_O	Electrochemical affinity for reduction
a	Lattice constant
B^{drag}	Drag coefficient
b	Magnitude of Burgers vector
b_a	Tafel slope for anodic reaction
b_c	Tafel slope for cathodic reaction
C_O	Concentration constants of oxidized species
C_R	Concentration constants of reduced species
E	Potential at working electrode
E_{corr}	Corrosion potential
E_{rp}	Repassivation potential
E_b	Breakdown potential
F	Faraday's constant
f_v	The volume fraction of activated micro- defects
h	Hardening modulus
I_{corr}	Corrosion current density
J_i	Fluxes of irreversible processes (i = 1,2,. . .)
$J_{M,a}$	The irreversible flux of anodic half-reaction of an oxidation process
$J_{M,c}$	An irreversible flux of cathodic half-reaction of the oxidation process
$J_{O,a}$	The irreversible flux of anodic half-reaction of the reduction process
$J_{O,C}$	Irreversible flux of cathodic half-reaction of reduction process
j_0	Exchange flux (current density)
j_M^0	Exchange flux of oxidation process
j_R^0	Exchange flux of reduction process
j_{Fe}^0	Exchange flux of metal dissolution
$j_{O_2}^0$	Exchange flux of oxygen evolution
k_B	Boltzmann constant
k_a	Anodic reaction rate constant
k_c	Cathodic reaction rate constant
k_h	Thermal conductivity
m_s	Molar mass
N_A	Avogadro's number
R	Universal gas constant
r	Internal friction (IF) generated heat
r^{drag}	IF due to the drag mechanism
r^{dis}	IF due to dislocation motion
Δs	Change of total specific entropy
S_{corr}	Entropy due to corrosion
S_{mec}	Entropy due to mechanical loading
S_{act}	Entropy due to activation overpotential
S_{react}	Entropy due to reaction overpotential
S_T	Entropy due to thermal conduction
S_r	Entropy due to internal friction
$S_{\mu p}$	Entropy due to microplasticity
υ_j	Chemical reaction rate
W	Disorder parameter
z	Effective charge number
z_M	Effective charge number for oxidation
z_O	Effective charge number for reduction
α_H	Taylor's constant
$\alpha_{M,a}$	Charge transfer coefficient of anodic half-reaction of an oxidation process
$\alpha_{M,c}$	Charge transfer coefficient of cathodic half-reaction of an oxidation process
$\alpha_{O,a}$	Charge transfer coefficient of anodic half-reaction of the reduction process
$\alpha_{O,c}$	Charge transfer coefficient of cathodic half-reaction of the reduction process
β_a	Tafel slope for anodic branch
β_c	Tafel slope for cathodic branch
$\dot{\gamma}$	Shear strain rate
$\boldsymbol{\varepsilon}_P^{\mu}$	Microscopic plastic strain tensor
η	Overpotential
μ	Shear modulus
v	Dislocation velocity
ρ	Mass density
ϱ	Total dislocation density
ϱ_m	Mobile dislocation density
σ_y	Microscopic yield stress (fatigue limit)
$\boldsymbol{\sigma}^{\mu}$	Microscopic stress tensor
ϕ	Thermodynamic state index
ϕ_{cr}	Critical thermodynamic state index
Ψ_f	Frequency coefficient

1. Introduction

Unified mechanics theory (UMT) has been extensively documented in the literature [1–8]. A summary is provided here, along with essential differences between UMT and Newtonian mechanics. Newtonian mechanics does not account for degradation and dissipation in the universal laws of motion. Those are governed by the laws of thermodynamics. Because the Newtonian space–time coordinate system does not have an axis for dissipation. To make laws of Newton thermodynamically consistent, traditionally, degradation and dissipation are introduced via empirical dissipation and degradation evolution functions. These empirical functions require curve fitting to dissipation, and degradation test data to obtain them. The dissipation constraint functions in Lagrangian mechanics are examples of empirical dissipation/degradation functions.

Unified mechanics theory (UMT) unifies Newton's universal laws of motion and the second law of thermodynamics at the ab-initio level [1]. In addition to the Newtonian space–time coordinates, a fifth linearly independent axis called the Thermodynamic State Index (TSI) is introduced based on Boltzmann's entropy formulation. It provides a physics-based life span prediction metric for any process without the need for curve fitting an empirical dissipation/degradation function, [1–8]. On the other hand, UMT relies on the analytically derived thermodynamic fundamental equation.

The thermodynamic state index of UMT is given by:

$$\phi_i = \phi_{cr}\left[1 - exp\left(\frac{-\Delta s_i \cdot m_s}{R}\right)\right] \tag{1}$$

where, m_s is the molar mass, R is the universal gas constant, Δs_i is the change in specific entropy according to the thermodynamic fundamental equation, ϕ_{cr} is a user-defined critical value of TSI. The thermodynamic life span of material travels between 0 when the entropy generation rate is maximum and 1, when the entropy generation rate is zero, along the Thermodynamic State Index (TSI) axis. The TSI evolution requires analytically deriving the thermodynamic fundamental equation which includes all entropy generation mechanisms in the process.

The continuum damage mechanics have been widely studied, for corrosion fatigue damage. However, these models rely on an empirical damage potential obtained by curve fitting to test data [9–12]. Each loading path, temperature range, loading frequency, sample size, boundary/initial conditions, and material requires a different damage potential. There is no damage potential in the unified mechanics theory.

This study aims to develop an UMT-based fatigue life prediction model for pre-corroded metals subjected to ultrasonic vibrations. The main focus here is the derivation of the thermodynamic fundamental equation for corrosion. The thermodynamic fundamental equation for metal fatigue has been validated in our recent published papers [6–7]. The corrosion thermodynamic fundamental equation used in this study has been formulated based on the product of thermodynamic fluxes and forces. Entropy generation mechanisms in the corrosion process have been studied in chemistry literature. However, they have never been used to formulate the thermodynamic fundamental equation needed for the unified mechanics theory to quantify the corrosion in a continuum mechanics problem. The details of the pre-corrosion preparation, the determination of necessary parameters for the computation of corrosion entropy generation using the Tafel test, the computation procedure for the corrosion entropy, the quantification of the total damage due to corrosion, and then ultrasonic vibration high cycle fatigue loading testing and simulations, are the main contributions in this study.

The term corrosion usually is used to describe an electrochemical reaction where the transfer of electrons from one chemical species to another happens. For example, it includes the oxidation process of metal that loses electrons and the reduction process of the species that receive electrons. Therefore, the corrosion referred to in this article refers to the so-called redox reaction.

In this study, NaCl aqueous solution was chosen as the corrosion media because steel reinforcement in reinforced concrete can be severely corroded in the presence of high chloride concentration due to the inherent porosity of concrete. This is a typical problem in locations where NaCl is spread over the roads to melt the snow in the winter, where highway bridge columns suffer from this problem severely.

In the test, metal samples were immersed in a 5 wt% sodium chloride (NaCl) solution at a pH of 7 to simulate corrosive conditions. The mechanical loading was applied by ultrasonic vibration, operating at 20 kHz with maximum nominal stress below the material's yield stress. Although the corrosion tests were performed before the ultrasonic vibration tests on the samples, their cumulative entropy production can be added together because entropy is an additive property [1]. In Section 2, the entropy generation equations for electrochemical corrosion and ultrasonic vibration are derived. In Section 3, the experimental procedures and test results are presented. In Section 4, the TSI evolution is computed to predict the fatigue life of the pre-corroded samples. Finally, the simulation results are compared with the test data.

2. Derivation of the thermodynamic fundamental equation

Entropy generation mechanisms can be divided into two categories: the first is the entropy generation due to corrosion, and the second is the entropy generation due to mechanical loading (ultrasonic vibrations). The entropy generation due to corrosion can be calculated by the multiplication of thermodynamic fluxes (corrosion current density) and thermodynamic forces (electrochemical affinity) in the form of Onsager reciprocal relations [13].

The ultrasonic vibration entropy generation formulation is published in reference [7]. Because entropy is an additive property, we can write the following equation for the total entropy production to obtain the thermodynamic fundamental equation,

$$\Delta S = \Delta S_{corr} + \Delta S_{mec} \tag{2}$$

where ΔS is the total entropy generation, ΔS_{corr} is the entropy generation due to corrosion, and ΔS_{mec} is the entropy generation due to mechanical loading.

2.1. Entropy generation due to electrochemical corrosion reaction

The entropy generation equation for metal corrosion has been extensively studied based on the theory of chemical kinetics and fundamentals of irreversible thermodynamics. Gutman (1998) [14] derived the entropy production equation for a simple oxidation reaction of Fe (metal dissolution) based on the activation overpotential, in the form of the sum of the product of thermodynamic fluxes and forces,

$$Fe \leftrightarrow Fe^{z^+} + ze^- \tag{3}$$

$$\Delta S_{act} = \frac{1}{T}\int_{t_0}^{t} (J_a \alpha_a \tilde{A} + J_c \alpha_c \tilde{A}) dt_{corr} \tag{4}$$

where Fe is the metallic electrode, e is the electron, z is the number of electrons involved in the electrochemical reaction, and the denominator T is the absolute temperature, t_{corr} is the corrosion time.

In equation (4), the thermodynamic fluxes refer to the anodic flux, J_a, and cathodic flux, J_c, from the Butler-Volmer equation while the thermodynamic forces refer to the corresponding chemical affinity $\tilde{A}$. The Butler-Volmer equation is given by [15–17].

$$J = J_a + J_c = j_0 \left[\exp\left(\frac{\alpha_a z F \eta}{RT}\right) - \exp\left(-\frac{\alpha_c z F \eta}{RT}\right) \right] \tag{5}$$

In equation (5), α_a and α_c are the charge transfer coefficients. It should be noted that for single-step reactions, $\alpha_a + \alpha_c = 1$. In this specific case, they are called symmetry factors [18]. F is Faraday's constant. η is the overpotential defined as $\eta = (E - E_{corr})$, in which E_{corr} is the equilibrium electrode potential (corrosion potential), E is the potential of the working electrode. The chemical affinity $\tilde{A}$ is defined as $\tilde{A} = z\eta F = zF(E - E_{corr})$, [14]. Finally, j_0 is the exchange flux, which is a function of the concentrations of the reduced and oxidized species:

$$j_0 = F(k_c C_O)^{\alpha} (k_a C_R)^{1-\alpha} \tag{6}$$

where k_a and k_c are the anodic and cathodic reaction rate constants, respectively. C_O and C_R are the concentration of oxidized and reduced species, respectively.

Imanian and Modarres (2015) extended equation (4) to a redox reaction, as follows [19–20],

$$\Delta S_{act} = \frac{1}{T}\int_{t_0}^{t} [J_{M,a}\alpha_M \tilde{A}_M + J_{M,c}(1-\alpha_M)\tilde{A}_M + J_{O,a}\alpha_O \tilde{A}_O + J_{O,c}(1 - \alpha_O)\tilde{A}_O] dt_{corr} \tag{7}$$

where $J_{M,a}$ and $J_{M,c}$ are the irreversible anodic and cathodic activation fluxes (thermodynamic fluxes) for oxidation reaction, $J_{O,a}$ and $J_{O,c}$ are the anodic and cathodic activation fluxes (thermodynamic fluxes) for reduction reactions, respectively. α_M and α_O are the charge transport coefficients for the oxidation reaction and reduction reaction, respectively. $\tilde{A}_M$ and $\tilde{A}_O$ are the electrochemical affinity (thermodynamic force) for oxidation and reduction reactions induced by the electrochemical potential, respectively. Equation (4) and (7) shows that the anodic and cathodic current

densities (in units of A/m^2) driven by the applied overpotential (in units of V) cause irreversible entropy production over time ($J \cdot K^{-1} \cdot m^{-2}$). The illustration shown in Fig. 1 explains the four different fluxes in equation (7).

The flux can be related to current density by using Faraday's second law as follows [19],

$$I_{M,a} = z_M F J_{M,a} \tag{8}$$

where $I_{M,a}$ is the anodic current density for the metal dissolution, z_M is the number of electrons involved in the metal dissolution reaction, $J_{M,a}$ is the irreversible anodic activation flux and F is Faraday's constant.

Imanian and Modarres (2015) [20] also proposed three additional entropy production mechanisms during the corrosion besides the activation overpotential. Among the four mechanisms, we only consider the entropy generation due to activation overpotential ΔS_{act} and the entropy generation due to chemical reaction overpotential ΔS_{react}. We do not consider the entropy generation due to diffusional overpotential ΔS_{conc} and ohmic loss ΔS_{Ω}. Because, the diffusional overpotential and the ohmic loss are negligible when the solution is well mixed (very low chemical concentration gradient) and when the electrolyte has a strong conductivity, respectively [21]. Therefore, these two mechanisms are trivial for the test conditions we imposed. The entropy production due to chemical reaction overpotential is given by

$$\Delta S_{react} = \frac{1}{T}\int_{t_0}^{t}\left(\sum_{j=1}^{r} \upsilon_j A_j\right) dt_{corr} \tag{9}$$

where r is the number of chemical reactions involved, T is the absolute temperature, υ_j is the chemical reaction rate in units of mol/s, A_j is the chemical reaction affinity in the units of kJ/mol.

Therefore, the total entropy production during the corrosion is given by,

$$\Delta S_{corr} = \Delta S_{act} + \Delta S_{react} \tag{10}$$

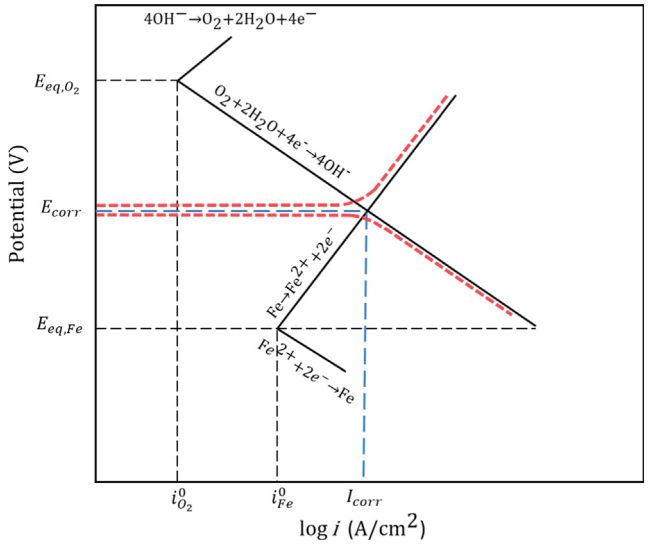

Fig. 1. Schematic showing the anodic and the cathodic parts of the iron corrosion reaction in a neutral electrolyte, adapted from Popov (2015) [17]. The red dashed line in the middle constructs the Tafel plot. Details of the Tafel plot will be discussed later in Section 3.2. (For interpretation of the references to colour in this figure legend, the reader is referred to the web version of this article.)

2.2. Required measurements for the calculation of corrosion entropy production

The corrosion behavior of steel in salt solution has been studied extensively [21–25]. The following reactions occur at the steel sample surfaces when ferrite is acting as the anode [16–17,23]:

On the anode side, loss of electrons occurs

$$Fe \leftrightarrow Fe^{2+} + 2e^{-}$$

On the cathode side, the evolution of dissolved oxygen

$$O_2 + 2H_2O + 4e^{-} \leftrightarrow 4(OH)^{-} \tag{11}$$

To compute the corrosion entropy production from reaction (11), the irreversible anodic and cathodic activation fluxes $J_{M,a}$ and $J_{M,c}$ for metal oxidation and the irreversible anodic and cathodic activation fluxes $J_{O,a}$ and $J_{O,c}$ for oxygen reduction must be determined. Using equation (5), they can be expressed as,

$$\begin{aligned} J_M &= J_{M,a} + J_{M,c} \\ &= j_M^0\left[\exp\left(\frac{\alpha_{M,a}\tilde{A}_M}{RT}\right) - 1\right] - j_M^0\left[\exp\left(\frac{-\alpha_{M,c}\tilde{A}_M}{RT}\right) - 1\right] \end{aligned} \tag{12}$$

$$\begin{aligned} J_{O,a} &= J_{O,a} + J_{O,c} \\ &= j_R^0\left[\exp\left(\frac{\alpha_{O,a}\tilde{A}_O}{RT}\right) - 1\right] - j_R^0\left[\exp\left(\frac{-\alpha_{O,c}\tilde{A}_O}{RT}\right) - 1\right] \end{aligned} \tag{13}$$

where j_M^0 and j_R^0 are the exchange flux for the oxidation reaction and reduction reaction, respectively. These exchange fluxes can also be expressed in the following form: $j_M^0 = j_{Fe}^0$, $j_R^0 = j_{O_2}^0$ according to the reaction in (11). $\alpha_{M,a}$, $\alpha_{M,c}$, $\alpha_{O,a}$, $\alpha_{O,c}$ are the charge transfer coefficients. $\tilde{A}_M$ and $\tilde{A}_O$ are chemical affinities related to overpotential.

Throughout reaction (11) and equations (12–13), we assume that the redox reaction during the electrochemical corrosion only involves the metal oxidation and the reduction of dissolved oxygen, and they both are single-step reactions that follow the symmetry property. Therefore,

$$\alpha_{M,a} + \alpha_{M,c} = 1;\ \alpha_{O,a} + \alpha_{O,c} = 1 \tag{14}$$

The effective charge coefficient $\alpha_{M,a}$ and $\alpha_{O,C}$ can be calculated based on the slope of the Tafel plot, [26–27],

$$\beta_a = \frac{2.303RT}{\alpha_a zF},\ \beta_c = \frac{2.303RT}{\alpha_c zF} \tag{15}$$

where coefficients β_a and β_c are the slopes of the two branches on the Tafel plot (Tafel slope, Tafel constant):

Exchange current density is a function of the concentrations of the reduced and oxidized species, as shown in equation (6). In the literature, they are given in the following range depending on the exposure conditions, [17,28],

$$j_{Fe}^0 = 10^{-4} \sim 10^{-5} A/cm^2,\ \ j_{O_2}^0 = 10^{-6} \sim 3 \times 10^{-7} A/cm^2 \tag{16}$$

We will use these ranges because as opposed to corrosion current densities, exchange current densities depend on the concentration of ionic species and are difficult to determine from corrosion experiments.

In summary, the calculation of corrosion entropy production requires the corrosion potential, corrosion currents, and charge transfer coefficients. In Section 3, the detailed procedure for the determination of these variables is discussed.

2.3. Entropy generation due to mechanical loading (ultrasonic vibration)

The entropy generation during ultrasonic vibration fatigue has been studied recently. There are six entropy generation mechanisms during very high cycle fatigue. However, it was shown that only three are dominant entropy generation mechanisms [7],

$$\Delta S_{mec} = \Delta S_T + \Delta S_r + \Delta S_{\mu p} \tag{17}$$

where ΔS_T is the entropy generation due to thermal conduction, ΔS_r is the entropy generation due to internal heat generation (drag mechanism and dislocation motion), and $\Delta S_{\mu p}$ is the entropy generation due to microplastic work at inclusions. They are given by the following equations,

$$\Delta S_T = -\int_{t_0}^{t} \left(k_h \frac{\nabla T \cdot \nabla T}{T^2} \right) dt \tag{18}$$

$$\Delta S_r = \int_{t_0}^{t} \frac{(\varrho B^{drag} v v + \frac{1}{2}\mu b^2 \dot{\varrho} - \alpha_H \mu b \sqrt{\varrho}\dot{\gamma})}{T} dt \tag{19}$$

$$\Delta S_{\mu p} = \int_{t_0}^{t} \Psi_f \left(\phi f_v \frac{\boldsymbol{\sigma}^{\mu} : \dot{\boldsymbol{\varepsilon}}_p^{\mu}}{T} \right) dt \tag{20}$$

where k_h is coefficient of heat conduction, ∇T is the temperature gradient, ρ is the mass density, r is the internal heat generation due to drag and dislocation motion mechanisms, B^{drag} and v represent the effective drag coefficient and velocity of dislocation, respectively. The terms μ, b, ϱ, and α_H are the shear modulus, the magnitude of Burger's vector, total dislocation density, and Taylor's hardening parameter, respectively. Ψ_f is an ultrasonic vibration frequency coefficient, ϕ is the thermodynamic state index, f_v is the activated volume fraction of micro-defects (inclusions, vacancies, dislocations), $\boldsymbol{\sigma}^{\mu}$ is **a** microscopic stress tensor, $\boldsymbol{\varepsilon}_p^{\mu}$ is the microscopic plastic strain tensor.

Equation (18) describes entropy production as the product of heat flux and temperature gradient. The heat flux and temperature gradient here are the thermodynamic flux and force, respectively, for the thermal conduction problem. Equation (19) shows the entropy production due to the phonon-dragging force $F_{drag} = B^{drag} v$ that impedes the dislocation motion moving at velocity v, and the entropy production due to motion of dislocation under a generation rate of $\dot{\varrho}$ and a shear strain rate of $\dot{\gamma}$. Equation (20) formulates the entropy production due to the microplastic work generated by the localized micro-stress $\boldsymbol{\sigma}^{\mu}$ and micro-strain $\boldsymbol{\varepsilon}_p^{\mu}$ at micro defects that evolute according to ϕ. The details of deriving equation (22–24) are thoroughly discussed in [7].

Compared to standard fracture mechanics problems where a pre-existing crack is introduced into the sample, the surface roughness/defects created during the corrosion test is at the submicron level. We should emphasize that in an ultrasonic test if there is a macro crack in the sample, it is not possible to run an ultrasonic vibration test. Because the ultrasonic vibration test occurs at the natural (resonance) frequency of the sample. If there is a crack propagating as in a fracture mechanics problem, it shifts the stiffness of the sample out of the resonance frequency. The ultrasonic vibration then stops causing the termination of the test [29]. Therefore, the thermodynamic fundamental equation for mechanical loading does not consider the entropy generation due to macrocrack propagation as in a fracture mechanics problem.

After the corrosion experiment, the samples were polished to a smooth surface to a certain degree. However, the remaining surface roughness/defects, cavities, and corrosion pits do accelerate the crack initiation process due to the stress concentration. They are considered using an average defect ratio f_v determined by SEM after the corrosion, which is implemented in the microplasticity model to represent the accelerated void nucleation rate that leads to faster crack initiation. It should be emphasized that we assume the laws of localization and homogenization in the gage section of the ASTM standard sample in this study. Calculations are done for this homogenized gage section in the middle. As a result, our calculations are essentially focused on a single point at the gage center, which is standard in the constitutive modeling community. This practice is also common in fatigue testing where the stress is assumed to be uniform at the gauge section. Then S—N curves are plotted for this homogenized stress value at the gauge section. In our experiments, all our samples broke at the gauge section. Therefore we assume this standard practice is reasonable.

3. Details of experiments

Samples for all tests described in this paper were made of non-alloy quality low-carbon structural steel (EU S355J2 + N [29], Equivalent to ASTM A656 [31]) that has a microstructure consisting of ferrite (bright particles) and pearlite (dark particles), as shown in Fig. 2. It's chemical composition and mechanical properties can be found in the standards [29–31]. Fig. 3 shows the geometry of the samples used.

The mechanical material properties of the test samples and their chemical composition have been studied extensively in our recent publication [7]. The required material constants for the calculation of mechanical entropy production such as the Yield strength, Young's modulus, Poisson's ratio, Thermal expansion coefficient, and fatigue limit were all obtained experimentally. Table 8 includes the material properties of the samples.

The experiments in this study can be divided into two regimes: the corrosion regime and then fatigue regime. The corrosion was induced by immersing steel samples in a salt solution for some time. Corrosion activities were monitored using two electrochemical corrosion measurement techniques (Tafel and cyclic polarization measurements) throughout and at the end of the corrosion experiment. The overpotential applied during the corrosion measurements was to obtain the electrochemical polarization parameters (i.e., charge transfer coefficients). The measurements were done by a potentiostat [32], and the analysis was performed on both the Tafel plot and the Cyclic Polarization Test (CPT) plot. The fatigue regime was performed by subjecting the corroded samples to ultrasonic vibration well below the material's yield stress.

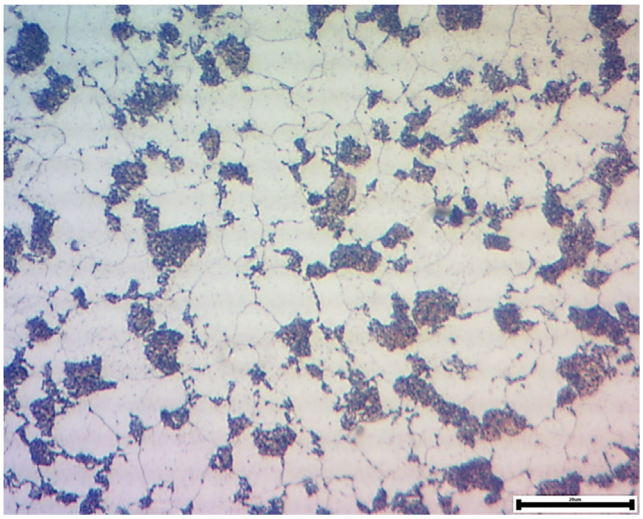

Fig. 2. SEM image of the microstructure after annealing.

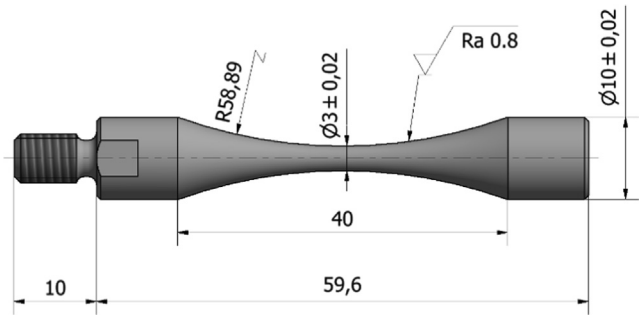

Fig. 3. Dimensions (in mm) of the specimens used for testing.

The fatigue S—N curve of the pre-corroded samples was obtained experimentally in this regime.

It is well understood that the synergistic interaction between concurrent fatigue loading and corrosion may result in the acceleration of damage. However, in this study, the corrosion and ultrasonic vibration high-cycle fatigue tests were performed separately. Because there is a big difference between the time required for the corrosion test and the high-cycle fatigue test. The corrosion test requires weeks to produce observable corrosion damage whereas the ultrasonic vibration fatigue fails the sample in two hours or less. Essentially, in this study, we are investigating the effect of corrosion damage on the ultrasonic vibration high cycle fatigue life of pre-corroded samples. Therefore our thermodynamic fundamental equation does not include an entropy generation term for concurrent corrosion-fatigue interactions.

3.1. Specimen preparation for corrosion experiment

The corrosion experiment requires a corrosion immersion test on the sample before the measurements of electrochemical parameters. As shown in Fig. 4, only the middle section (gauge length of about 14 mm) of the sample was exposed to the salt solution. Fig. 4 shows that the grip portion of the sample is coated with double-layer epoxy to protect it from being directly exposed to corrosive agents (chloride ions).

Fig. 4 (a) shows the test specimen. The copper wire welded to the top of the specimen is connected to the working electrode terminal of the potentiostat. Fig. 4 (b) illustrates the electroplating tapes. Fig. 4 (c) shows the double epoxy layer on top of the electroplating tapes after solidification.

3.2. Corrosion experiment

3.2.1. Corrosion immersion test

The corrosion parameters obtained from measurements such as the corrosion potential, corrosion current, and corrosion rate are not constant during the different stages of the corrosion process. Typically, the corrosion rate for steel is high at the initial stage of the corrosion, followed by a steady decline due to the formation of the rust layer that protects the sample from further corrosion. In the later stages of corrosion, the corrosion rate increases again with further exposure to chloride ions [33–34], because the rust layer becomes loose and porous after long-term immersion which weakens the protective rust layer. In addition, the rust layer breaks down by Cl-ions unevenly during a long immersion time, which opens new channels for the diffusion of iron ions into the salt solution [33,35–38].

Fig. 5 (b) shows that after a long immersion time in the salt solution, some iron rust that had formed on the surface of the samples broke down and fell into the salt solution.

Fig. 6 (a) shows that rust was formed uniformly on the exposed surface of the samples (gauge part) after 20 days of immersion in 5 wt% NaCl solution. However, after further immersion, the rust layer broke down unevenly, opening channels for the diffusion of iron ions in an anodic reaction, Fig. 6 (b).

3.2.2. Corrosion measurements

To validate the variation of electrochemical polarization parameters (such as corrosion current density, corrosion potential, and charge transfer coefficients) with respect to corrosion time, in this experiment, 3 sets of tests were performed consecutively to obtain sufficient data. A total of 16 samples were used (+1 control sample in tap water). All of them were immersed in a 5 % NaCl solution, as mentioned in the previous section. Tafel tests were performed at the beginning, after 20 days, and after 40 days for all samples. The cyclic polarization test (CPT) was performed once at the end of the experiment only for one sample. We ran a CPT test to obtain electrochemical evidence that the pitting corrosion had already begun (specimens should have been sufficiently damaged by corrosion before fatigue testing can begin).

The corrosion measurements in this study were all done by the potentiostat. The potentiostat [39–42] is a three-electrode system composed of a reference electrode (RE), a counter electrode (CE), and a working electrode (WE). Fig. 7 shows the setup of the electrochemical cell, in which the central test specimen (A656 grade steel) was the working electrode (WE), a rolled-up stainless steel wire mesh encircling the test sample was the counter electrode

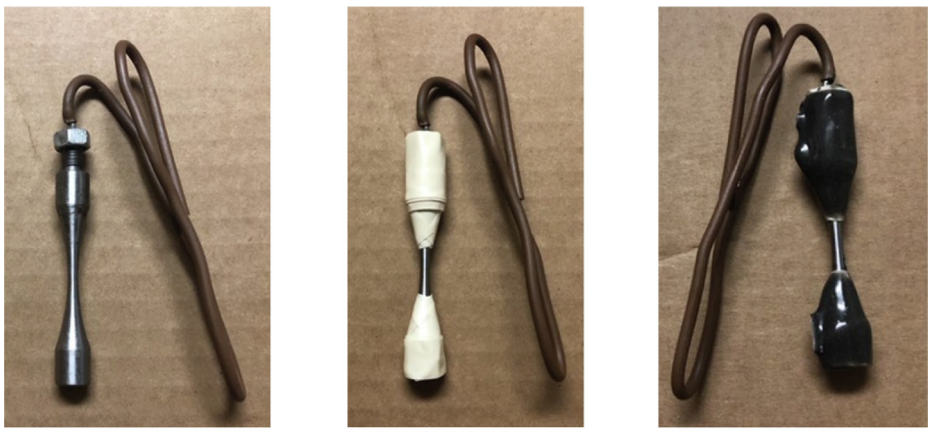

Fig. 4. Specimen preparation for corrosion testing.

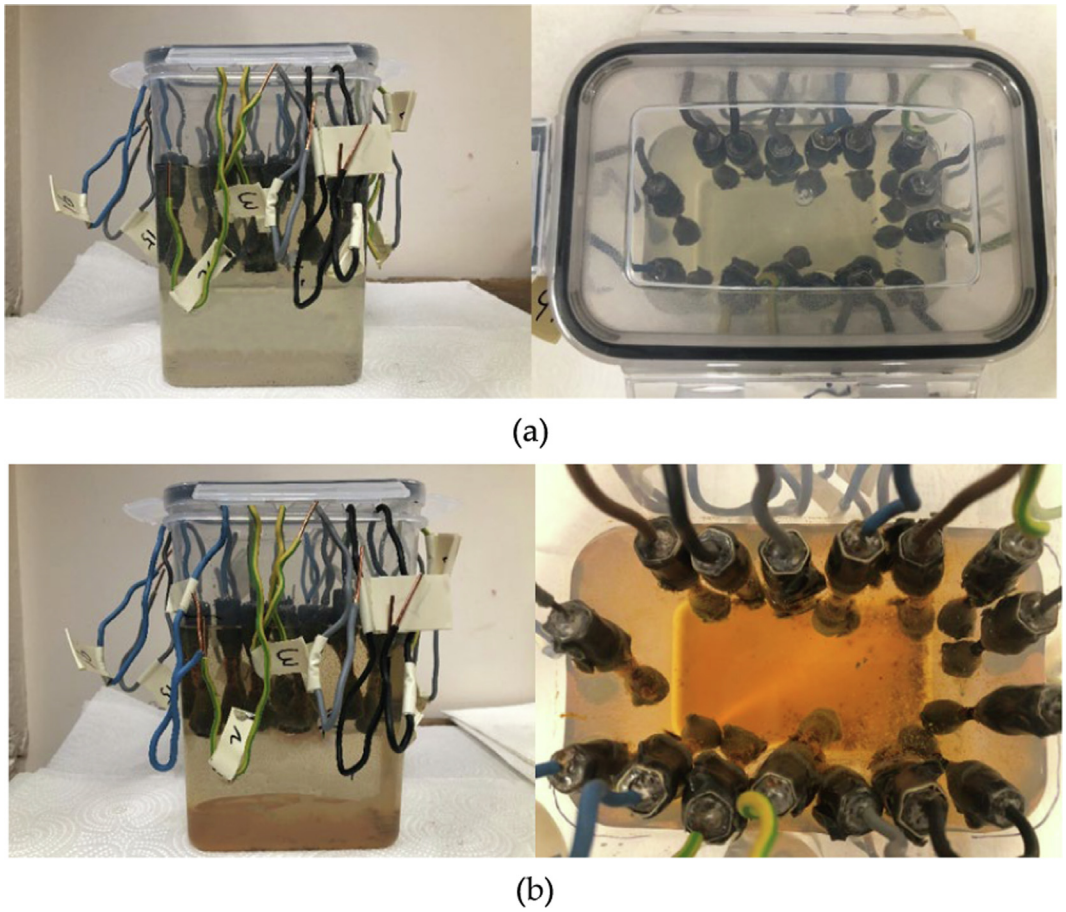

Fig. 5. Side and top view of the corrosion immersion test container at, (a) the beginning and (b) after 40 days.

Fig. 6. Enlargement of the gauge section after (a) 20 days, (b) 40 days of immersion in 5 wt% NaCl solution and (c) after the rust layer is removed by a wire brush.

(CE), and a saturated copper–copper sulfate electrode (CSE) was the reference electrode (RE) [43–45].

The potential between the WE and RE when no external potential or current is applied is defined as the open circuit potential (OCP). For Tafel tests, a potential shift of ±250 mV with respect to OCP is required. Therefore, the initial and final potential is set to be −250 mV and 250 mV with respect to the OCP, respectively. The scan rate is fixed at 0.167 mV/s [46–47]. The sample surface area, density, and equivalent weight are 1.613 cm^2, 7.87 g/cm^3, and 27.92 (unitless).

The CPT can be considered as the extension of the Tafel test. While the Tafel test only requires the potential shift of ±250 mV from OCP, the cyclic polarization test usually extends the potential shift in an anodic direction from −250 mV to + 1000 mV and then decreases toward the OCP. The purpose of performing the CPT is only to evaluate the susceptibility of the corroded sample to localized corrosion such as pitting corrosion [42]. To calculate the corrosion entropy production, we do not need parameters from the CPT.

3.2.3. Tafel results and discussion

The Tafel test results for 16 samples at the initial stage of corrosion (0 days of immersion time) are shown in Fig. 8. The electrochemical constants such as corrosion current, corrosion potential,

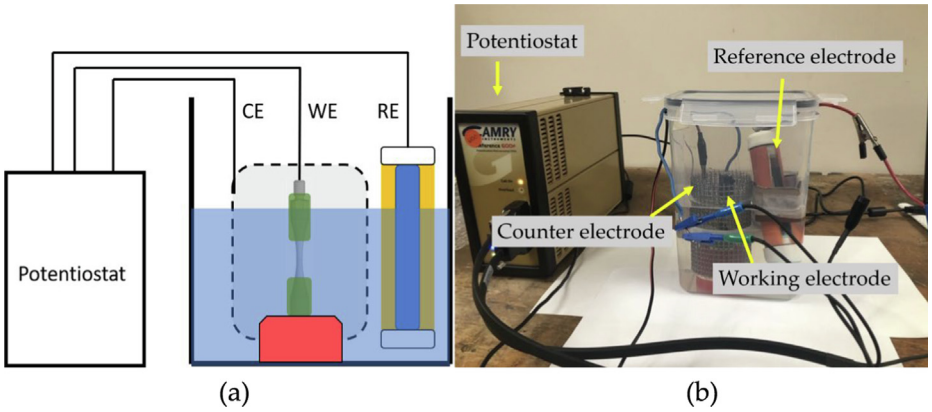

Fig. 7. (a) Schematic illustration of the electrochemical cell. (b) Photograph of the electrochemical cell.

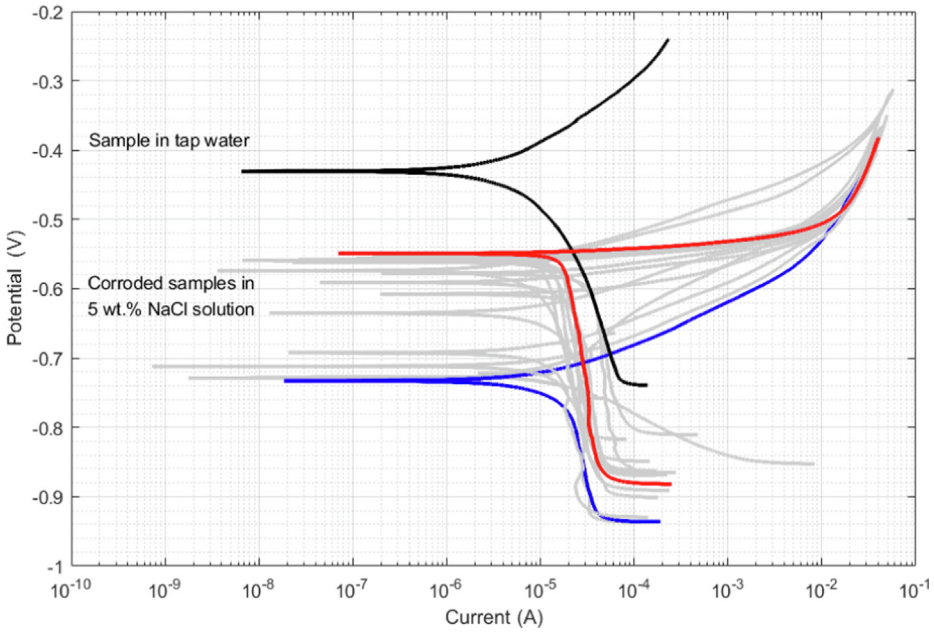

Fig. 8. Tafel plot of the 16 samples at the initial stage of corrosion. The black line denotes the sample measured in the tap water, as a benchmark. The red line denotes the sample with the highest corrosion potential, the blue line denotes the sample with the lowest corrosion potential. (For interpretation of the references to colour in this figure legend, the reader is referred to the web version of this article.)

and corrosion rate obtained from the Tafel fit function using Gamry Echem Analyst software are summarized in Table 1. The Tafel fit function requires the selection of both anodic and cathodic curves on the Tafel plot. Then the automatically produced intersection of the two extrapolation lines by the program gives the necessary results. However, the electrochemical constants can also be determined by manually extrapolating one curve (usually the cathodic curve) to the horizontal line at zero overpotential. This technique is called the E-log I method. It is sometimes required because when the anodic region has concentration affects the Tafel fit function becomes inaccurate. In this study, we use both approaches to obtain the electrochemical constants and compared the values.

Among 17 branches, only one branch was measured in tap water (black line); the rest were measured in 5 wt% NaCl aqueous solution. The tap water branch shows more positive corrosion potential, a smaller corrosion current, and a lower corrosion rate than the other branches. As a result of the low concentration of corrosive ions (chlorides) in tap water, this observation is to be expected and we used this branch as a benchmark for the rest of the Tafel measurements.

The corresponding Tafel plots for samples after 20 days and 40 days of immersion are shown in Figs. 9 and 10, respectively. The obtained electrochemical polarization parameters are summarized in Tables 2 and 3, respectively.

The Tafel plots in Figs. 8-10 show a certain degree of scatter. To obtain the mean electrochemical parameters of these test samples at different stages of corrosion with higher accuracy, we define the outliers as samples having values outside the normal distribution with a cutoff of 2 standard deviations from the mean. Those outliers are excluded from the calculation. Table 4 shows the mean electrochemical polarization parameters at different stages of corrosion. Despite that the electrochemical parameters obtained using the Tafel extrapolation method may have an inherent error, this method is acceptable and has been adopted in many highly cited papers [48–52].

Table 1
The electrochemical polarization parameters of 16 uncorroded samples were obtained from Tafel extrapolation. The units are V, V/decade, V/decade, μA, mV, and μpy, respectively.

Sample no	OCP	beta A	beta C	Icorr	Ecorr	Corr rate
1	−0.5618	0.0473	0.1345	15.6	−558	112.30
2	−0.5674	0.0426	0.3432	7.7	−574	59.75
3	−0.5997	0.0134	0.6531	11.3	−556	81.12
4	−0.6878	0.0159	0.5866	11.1	−556	80.20
5	−0.6515	0.0276	1.7140	27.4	−608	190.30
6	−0.6156	0.0244	1.1470	35.6	−577	256.00
7	−0.6186	0.0231	0.8987	22.7	−591	163.30
8	−0.6049	0.0609	0.5900	28.5	−666	205.30
9	−0.6152	0.0128	0.8840	18.9	−560	135.70
10	−0.6321	0.0116	1.1920	20.5	−552	147.40
11	−0.6134	0.0494	0.2760	13.5	−635	97.14
12	−0.6182	0.0147	0.9600	17.4	−562	125.20
13	−0.6873	0.0665	0.7608	19.8	−733	142.70
14	−0.6802	0.0596	1.3660	19.0	−692	142.00
15	−0.6201	0.0131	0.9531	14.4	−552	103.60
16	−0.6416	0.0644	1.3620	25.1	−712	187.20
mean	−0.6260	0.0342	0.8638	19.3	−605	139.33
Standard deviation	0.0359	0.0203	0.4172	7.09	60.5	50.454

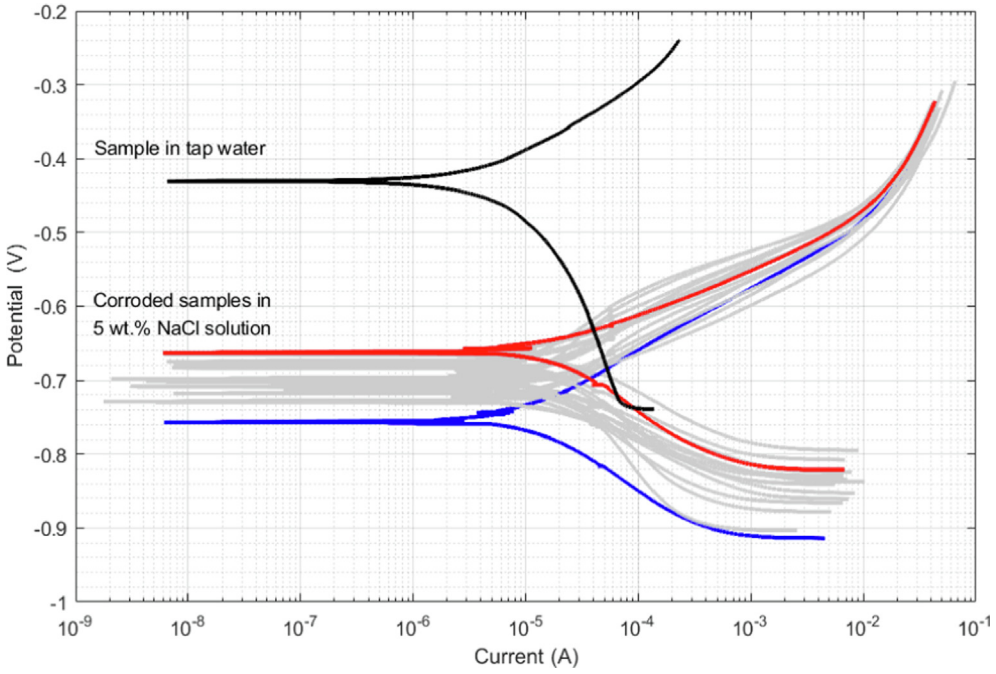

Fig. 9. Tafel plot of the 16 samples (after corrosion immersion test for 20 days) in 5 wt% NaCl solution.

Figs. 11 to 13 show the mean corrosion potential, mean corrosion current, and mean corrosion rate of 16 test samples as a function of corrosion immersion time. It is shown that the mean corrosion potential tends to reach a steady-state value after 20 days. On the other hand, the mean corrosion current and rate first tend to decrease and then increase. The error bars in these three figures visualize the minimum and maximum values.

The following observations can be made from Figs. 8 to 13, and Table 4:

1. The mean corrosion current for the samples decreased from the initial 18.8 μA to 11.9 μA after 20 days of immersion and then eventually increased to 68.2 μA after 40 days of immersion. The mean corrosion rate for the samples also follows the same pattern, which decreased from the initial 135.7 μpy to 86.6 μpy after 20 days of immersion, and then eventually increased to 493.1 μpy after 40 days of immersion. It was also observed that some samples after 40 days of immersion could have a corrosion rate of up to 1120.0 μpy (as shown in the rightmost error bar in Fig. 13), which is about six times its initial corrosion rate. The increment may indicate the initiation of pitting corrosion, as shown in Fig. 6 (c) and the SEM images in Section 3.3.2.
2. Tafel plots can be classified as either activation or diffusion-controlled [53]. Fig. 8 shows that at the initial stage of corrosion, the cathodic electrode reaction is under the diffusion control of dissolved oxygen. In contrast, the anodic electrode reaction undergoes electrochemically active dissolution under charge transfer (current) control. After forming the rust layer, the Tafel plot becomes activation-controlled (Figs. 9 and 10).

As pointed out in the literature [21,33,35–38], the decrease in corrosion rate can be attributed to the formation of a passive rust layer that mainly consists of $\alpha - FeO(OH)$ and $\gamma - Fe_2O_3/Fe_3O_4$. However, after further immersion time, the rust layer is either

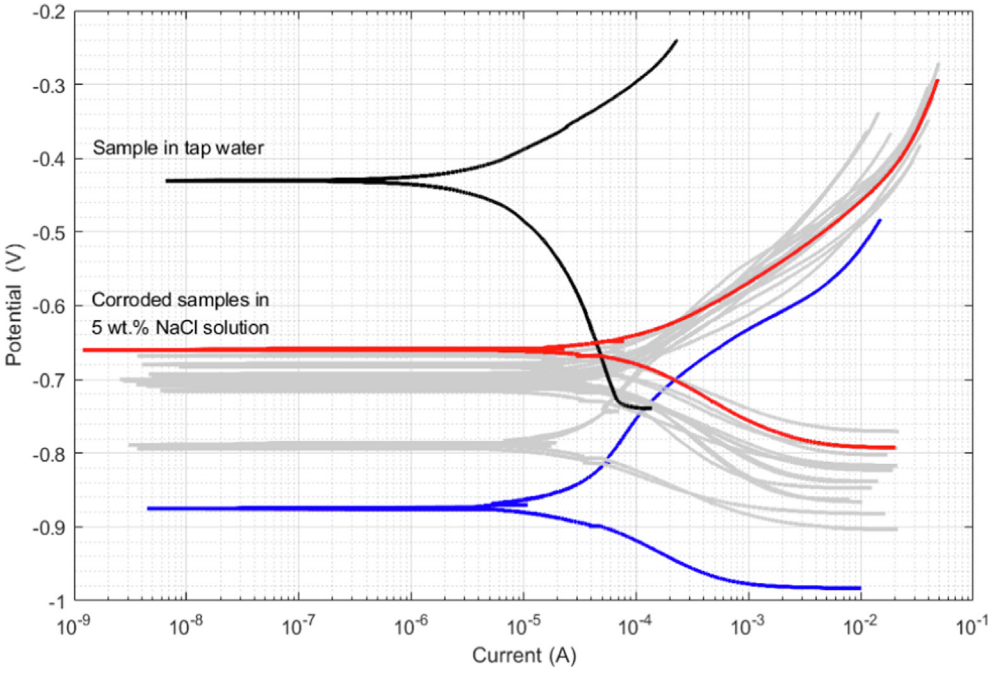

Fig. 10. Tafel plot of the 16 samples (after corrosion immersion test for 40 days) in 5 wt% NaCl solution.

Table 2
The electrochemical polarization parameters of 16 corroded samples (after 20 days of corrosion time) were obtained from Tafel extrapolation.

Sample no	OCP	beta A	beta C	Icorr	Ecorr	Corr rate
1	−0.5454	0.0623	0.0666	13.2	−664	94.91
2	−0.5580	0.0662	0.0637	8.1	−674	62.61
3	−0.5747	0.0722	0.0511	8.1	−701	58.59
4	−0.6288	0.0810	0.1611	29.2	−708	202.90
5	−0.5880	0.0700	0.0606	7.6	−699	53.02
6	−0.5906	0.0737	0.0975	12.7	−683	91.67
7	−0.6166	0.0846	0.0977	15.4	−717	110.90
8	−0.6030	0.0759	0.0516	7.3	−727	52.44
9	−0.6642	0.0853	0.0856	7.8	−756	55.96
10	−0.5806	0.0653	0.1056	15.1	−678	109.00
11	−0.6539	0.0725	0.1942	26.7	−712	192.50
12	−0.5849	0.1063	0.0577	8.0	−708	57.54
13	−0.5801	0.1129	0.0746	8.2	−697	58.96
14	−0.6109	0.0752	0.0622	9.9	−729	74.28
15	−0.5917	0.0951	0.0824	12.3	−701	88.34
16	−0.5722	0.0687	0.1248	23.6	−662	176.10
mean	−0.5965	0.0792	0.0898	13.3	−701	96.23
Standarddeviation	0.0311	0.0141	0.0393	6.92	24.3	49.251

Table 3
The electrochemical polarization parameters of 16 corroded samples (after 40 days of corrosion time) were obtained from Tafel extrapolation.

Sample no	OCP	beta A	beta C	Icorr	Ecorr	Corr rate
1	−0.7337	0.2075	0.0718	27.5	−875	197.90
2	−0.6325	0.1517	0.0551	24.1	−793	186.90
3	−0.5675	0.0947	0.0605	36.2	−715	260.70
4	−0.6539	0.1648	0.0625	27.8	−788	193.60
5	−0.5427	0.0792	0.0916	84.8	−659	589.80
6	−0.5435	0.1101	0.0967	89.5	−679	644.00
7	−0.5213	0.1113	0.0728	96.6	−667	695.50
8	−0.5885	0.1650	0.1656	155.0	−696	1115.00
9	−0.5982	0.0809	0.1492	73.5	−704	529.40
10	−0.5735	0.1026	0.0612	40.3	−707	289.90
11	−0.5424	0.1207	0.0734	119.0	−682	857.30
12	−0.5680	0.1229	0.0626	59.4	−709	428.00
13	−0.5726	0.1237	0.0790	55.7	−697	401.00
14	−0.6134	0.1459	0.1679	108.0	−693	804.70
15	−0.5528	0.1103	0.0712	75.6	−682	544.10
16	−0.5887	0.1088	0.0902	71.2	−701	531.60
mean	−0.5871	0.1250	0.0895	71.5	−715	516.84
Standarddeviation	0.0508	0.0331	0.0363	35.73	54.5	257.948

Table 4
The mean electrochemical polarization parameters of 16 samples at different stages of corrosion.

Set	1	2	3
Corrosion time	0 days (uncorroded)	20 days	40 days
β_A (V/decade)	0.0330	0.0738	0.1140
β_C (V/decade)	0.7846	0.0788	0.0789
Icorr (μA)	17.3615	12.1014	65.6692
Ecorr (mV)	−597.3846	−694.6181	−706.3846
Corr rate (μpy)	126.1700	88.2026	473.2154

* μpy = Microns per year

removed or becomes loose and porous, leading to a decrease in corrosion protection and an increase in corrosion rate.

3.2.4. CPT results and discussion

From the discussion in the previous section, a massive increment in corrosion rate after 40 days of corrosion immersion may indicate the occurrence of pitting corrosion. The cyclic polarization test (CPT) was performed on one corroded sample to validate this assumption.

Fig. 14 shows the CPT plot for one of the test samples (sample No. 1). Positive hysteresis is observed when the current density of the anodic back scan is larger than the current density of the original forward anodic scan. It has been shown that positive hysteresis indicates the initiation of pitting corrosion and a breakdown of the passive film on the metal surface [53], which matches our observations (Fig. 6). A review of passive layer breakdown on metal surfaces was published by Parangusan et al. (2021) [33].

In Fig. 14, E_b is the breakdown potential, E_{rp} is the repassivation potential, at which the current density returns to zero on a logarithmic scale, and E_{corr} is the corrosion potential. The potential difference between E_b and E_{corr} is related to the resistance of the test sample to pitting potential. It is clearly shown that the CPT plot is an extension of the Tafel plot beyond + 250 mV from OCP. They matched well in the linear polarization resistance (LPR) regime.

3.3. Ultrasonic vibration fatigue experiment

3.3.1. Fatigue test results

Ultrasonic fatigue tests were performed on the pre-corroded samples after completing corrosion immersion tests (12 samples from the set described in Section 3.2) and on a set of uncorroded reference samples (13 samples). The samples were polished to a smooth surface to remove the rust before the ultrasonic vibration fatigue test.

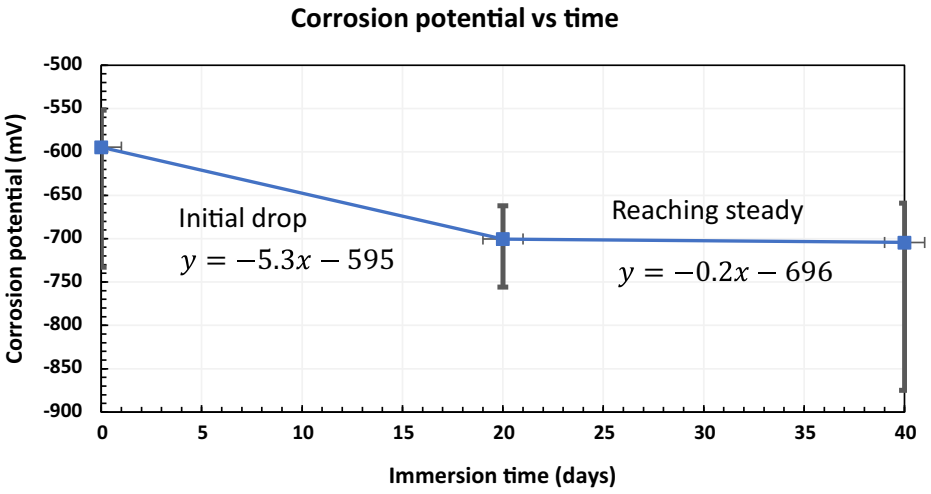

Fig. 11. Mean corrosion potential of 16 samples as a function of time.

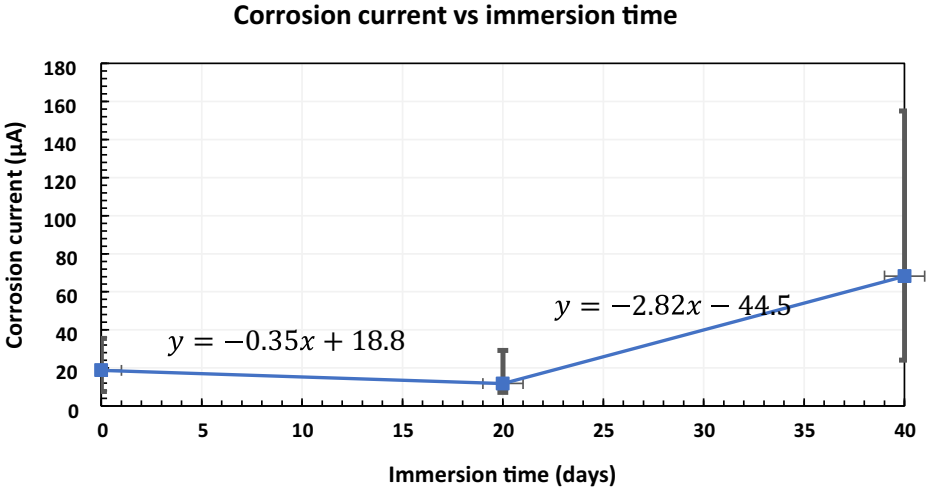

Fig. 12. Mean corrosion current of 16 samples as a function of time.

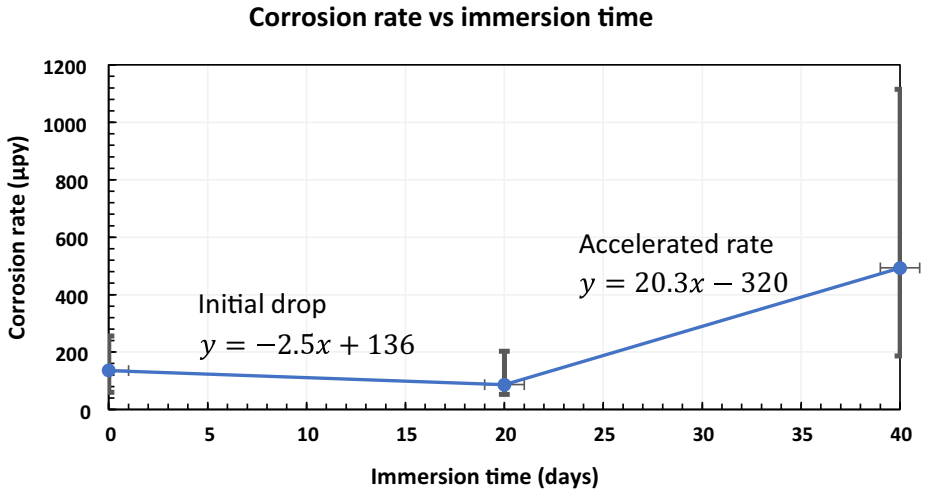

Fig. 13. The mean corrosion rate of 16 samples as a function of time.

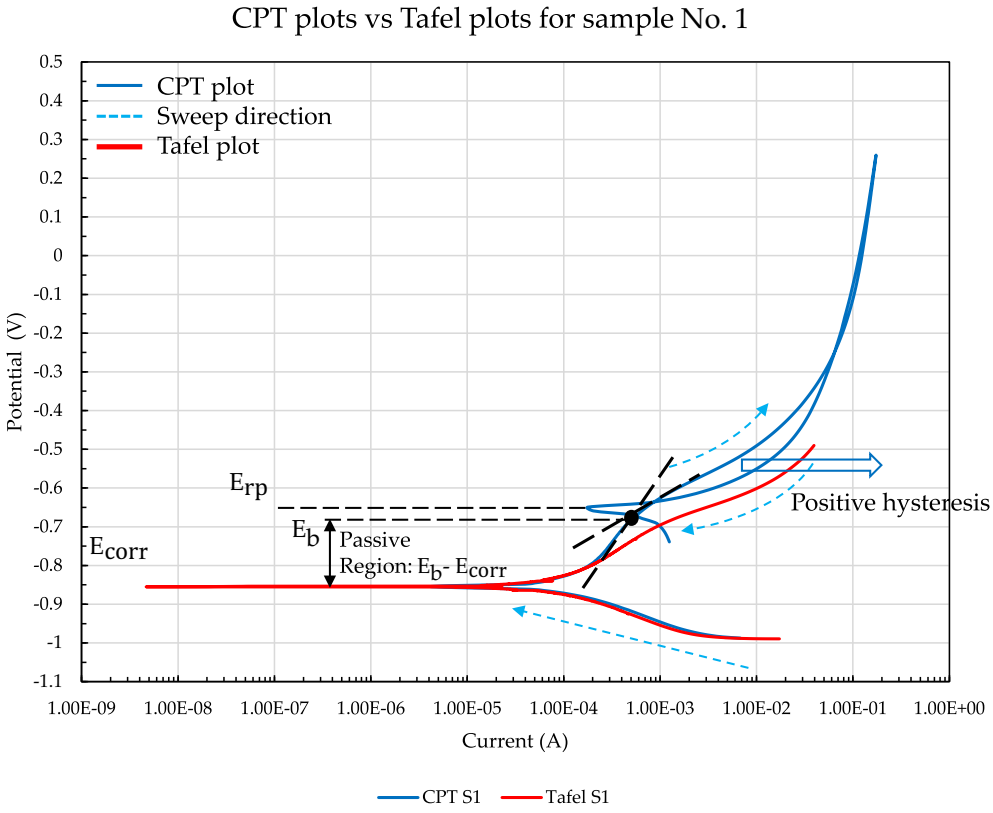

Fig. 14. Tafel and CPT plots for Sample No. 1.

Fatigue tests were performed utilizing the ultrasonic resonance testing machine ItalSIGMA MU26 which generates harmonic sinusoidal longitudinal vibrations with a frequency of 20 ± 0.5 kHz with a stress ratio of R = -1.

The high-cycle fatigue life data for uncorroded and pre-corroded samples are collects in Table 5. The fatigue data regression curves of uncorroded and pre-corroded samples were obtained after statistical analysis, as shown in Fig. 15 and Fig. 16. The X-axis is the number of cycles to failure while the Y-axis is the stress amplitude applied at the sample's gauge center. It can be observed that pre-corrosion reduces the fatigue life significantly and decreases the fatigue limit of the material (approximately 368 MPa to 354 MPa).

3.3.2. Fractography analysis of the corroded samples

The SEM images of the pre-corroded samples were recorded using a JEOL JSM-6480LV microscope and focusing on the fracture surface. It is shown that the saltwater corroded the surface and grain boundaries, as a result degrading the material, and causing the increase of initial micro-defects before the fatigue tests. As observed from the SEM images, the volume fraction of defect sites increases after corrosion due to the diffusion of chloride ions inside the samples. Under the same stress amplitude, the higher degree of

Table 5
The high-cycle fatigue tests results for uncorroded and pre-corroded samples.

Sample No.	Type of sample	Load level, MPa	Fatigue life, cycles
S355-006	uncorroded	370	8,291,418
S355-009		380	6,535,521
S355-010		370	6,175,451
S355-014		370	8,935,938
S355-017		380	6,111,314
S355-020		370	7,581,113
S355-022		370	7,804,534
S355-023		400	2,182,435
S355-024		400	2,863,719
S355-025		400	2,372,815
S355-026		390	5,008,228
S355-027		390	3,871,497
S355-028		390	3,369,247
S355-Corr_003	corroded	380	1,122,296
S355-Corr_004		360	5,493,802
S355-Corr_005		400	1,207,454
S355-Corr_006		380	1,236,010
S355-Corr_007		360	9,725,225
S355-Corr_008		400	2,862,939
S355-Corr_009		380	6,044,868
S355-Corr_010		360	16,347,710
S355-Corr_012		390	2,590,447
S355-Corr_013		390	707,339
S355-Corr_014		370	7,228,455
S355-Corr_015		370	2,504,304

corrosion, the shorter the fatigue life. Especially, this is more visible at higher stress levels. SEM images are also used to verify that there is no macrocrack on the surface that would make the study a standard fracture mechanics problem.

Fig. 17 (a) shows the fracture surface of the specimen tested at the highest stress level used in the tests (400 MPa) and characterized by single fatigue crack initiation site placed in a corrosion pit (Fig. 17 (c)). For comparison, Fig. 18 (a) shows an example of a specimen tested at the same stress level but with multiple fatigue crack initiation sites at different locations around the circumference. The fatigue life of this specimen was approximately 18 times lower than the previous one. The specimen from Fig. 17 has a flat fracture surface, while in the case of the specimen from Fig. 18 multiple parallel steps are visible. These typical images of the pre-corroded samples have been compared with the images of the uncorroded samples (Fig. 19). As it can be seen, in the case of samples exposed to a prior corrosive environment, the nature of their fracture changes significantly. For uncorroded samples for stress levels between 390 MPa and 400 MPa, the fracture surface appearance is comparable to a typical cup-cone fracture of a ductile material tested in tension (Fig. 19). The characteristic dimples are visible in the center of the fracture surface (Fig. 19 (b)). The corrosive environment causes the fracture to be brittle in this case.

Much smaller differences occur for stress levels lower than 380 MPa. The fractures of both pre-corroded and uncorroded specimens have brittle nature (Figs. 20 and 21). In the case of corroded specimens, the places of crack initiation are located in a corrosion pit (Fig. 20 (c)). In the case of uncorroded specimens, cracks initiate at surface defects (Fig. 21 (b)). For uncorroded specimens, fatigue striations are more pronounced at the fracture surface.

4. Thermodynamic state index (TSI)

The evolution of TSI is based on the cumulative specific entropy, Δs production. Δs is the summation of all entropy generation mechanisms discussed above.

$$\Delta s = \frac{1}{\rho}\left(\Delta S_{corr} + \Delta S_{mec}\right) = \frac{1}{\rho}\left(\Delta S_{act} + \Delta S_{react} + \Delta S_T + \Delta S_r + \Delta S_{\mu p}\right)$$

$$\Delta s = \frac{1}{\rho T}\int_{t_0}^{t}\Big[J_{M,a}\alpha_M\tilde{A}_M + J_{M,c}(1-\alpha_M)\tilde{A}_M + J_{O,a}\alpha_O\tilde{A}_O + J_{O,c}\Big(1-\alpha_O\Big)\tilde{A}_O\Big]dt_{corr}$$

$$+\frac{1}{\rho T}\int_{t_0}^{t}\Big(\sum\nolimits_{j=1}^{r}\upsilon_j A_j\Big)dt_{corr}$$

$$-\int_{t_0}^{t}\left(k_h\frac{\nabla T\cdot\nabla T}{\rho T^2}\right)dt + \int_{t_0}^{t}\left[\frac{r^{drag}+r^{dis}}{T}\right]dt + \int_{t_0}^{t}\Psi_f\left(\phi f_v\frac{\boldsymbol{\sigma}^{\mu}:\dot{\boldsymbol{\varepsilon}}_P^{\mu}}{\rho T}\right)dt \tag{21}$$

The degradation of the material happens according to the second law of thermodynamics which is the basis for the thermodynamic fundamental equation of the material and progresses

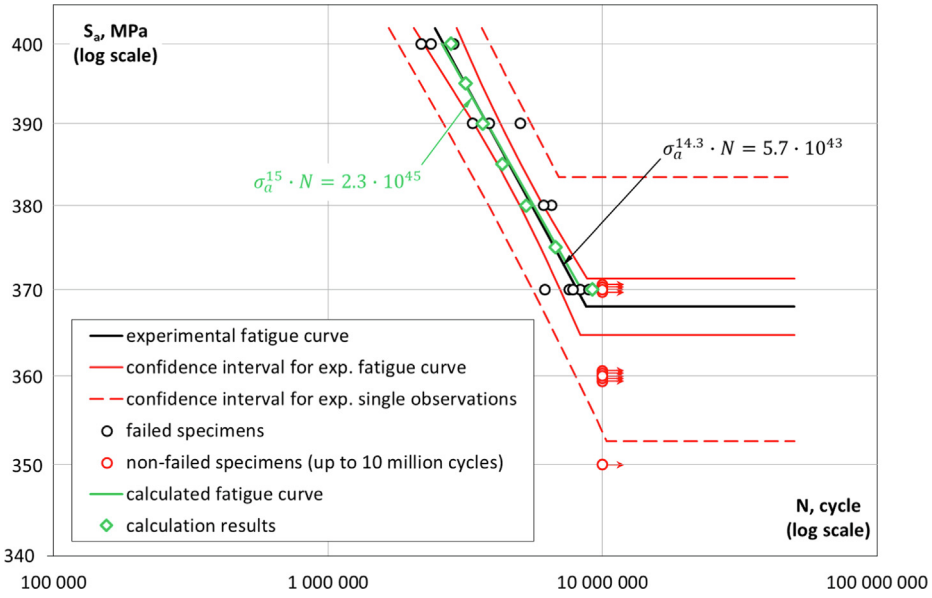

Fig. 15. Comparison of the experimental fatigue S—N data and simulations for the uncorroded samples [7].

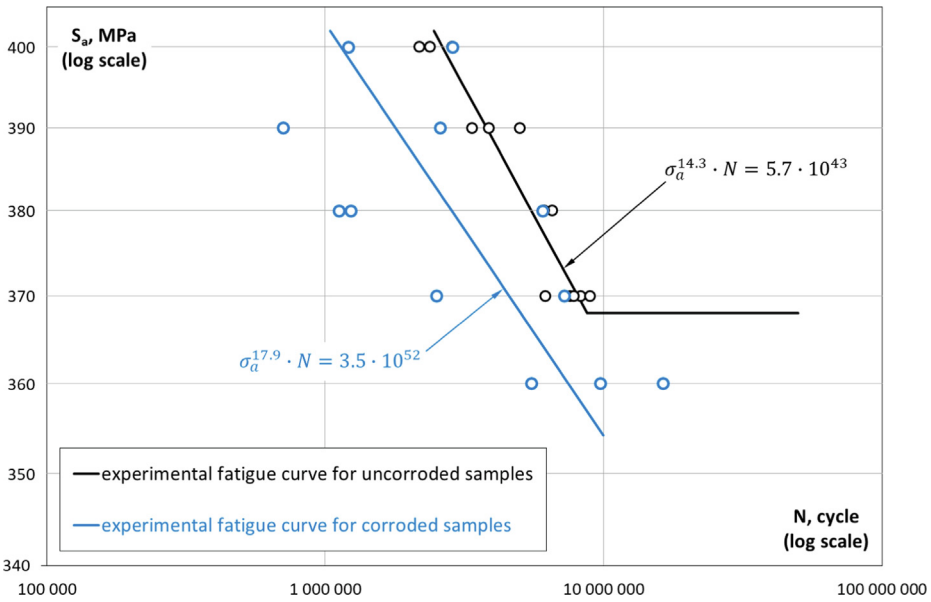

Fig. 16. Experimental fatigue S—N data for the uncorroded samples and pre-corroded samples.

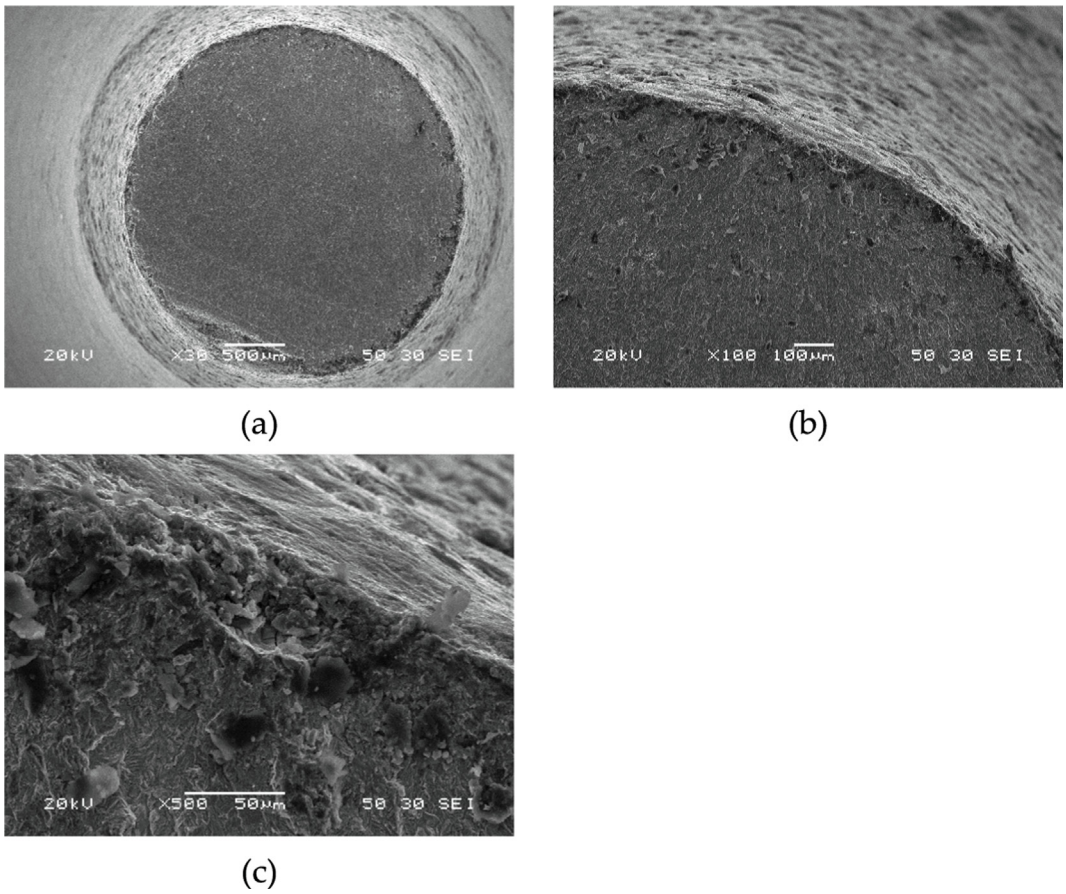

Fig. 17. SEM fractography of the pre-corroded samples after 2.8 million cycles at 400 MPa.

along the TSI axis between 0 and near 1. In practice, a critical value of TSI ϕ_{cr} is defined as a threshold because TSI is an exponential function. Hence never reaches precisely 1. In this study $\phi_{cr} = 0.97$ is used. We believe this value provides sufficient precision because it indicates that the probability of reaching maximum entropy at this state is 97 %.

In this study, we did not perform the corrosion test and ultrasonic vibration fatigue test concurrently. Therefore, the existence of an entropy generation term for corrosion-fatigue interactions is not included. However, there is a (weak) coupling between both phenomena through the thermodynamic state index present in the expression for the entropy production due to fatigue, as shown in

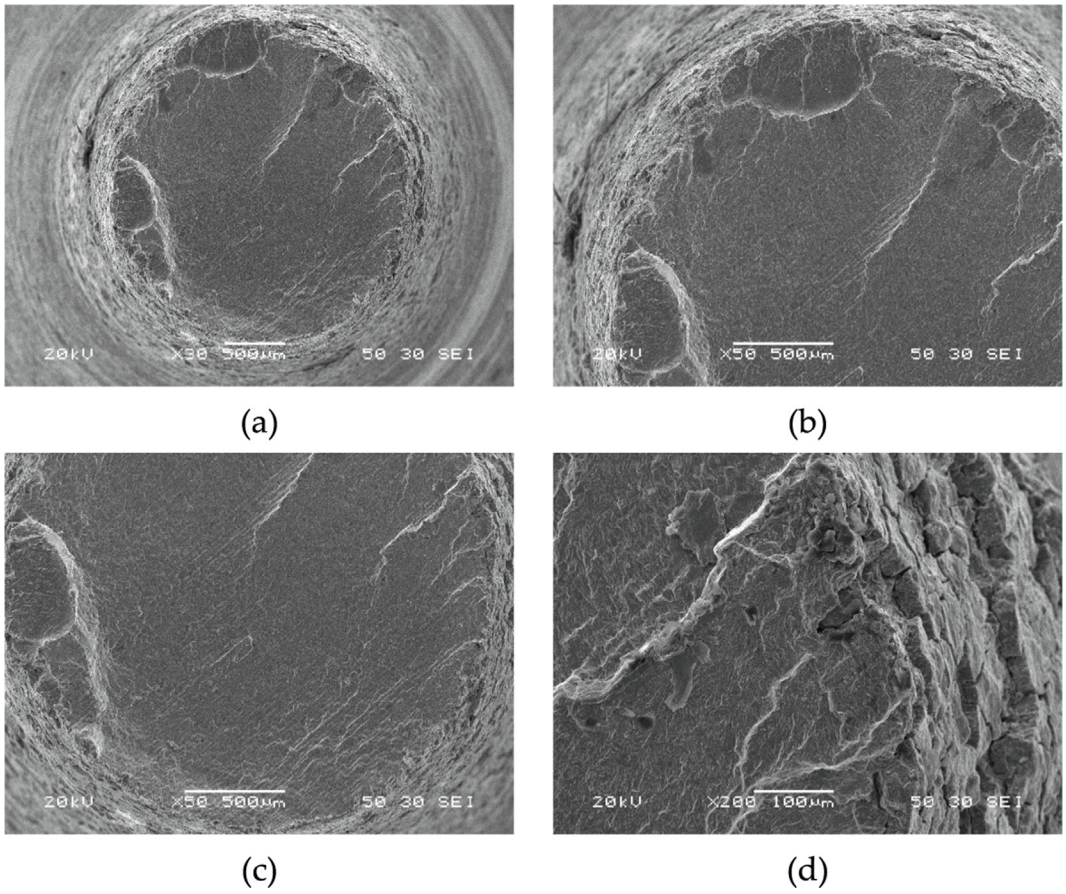

Fig. 18. SEM fractography of the corroded sample after 157 thousand cycles at 400 MPa.

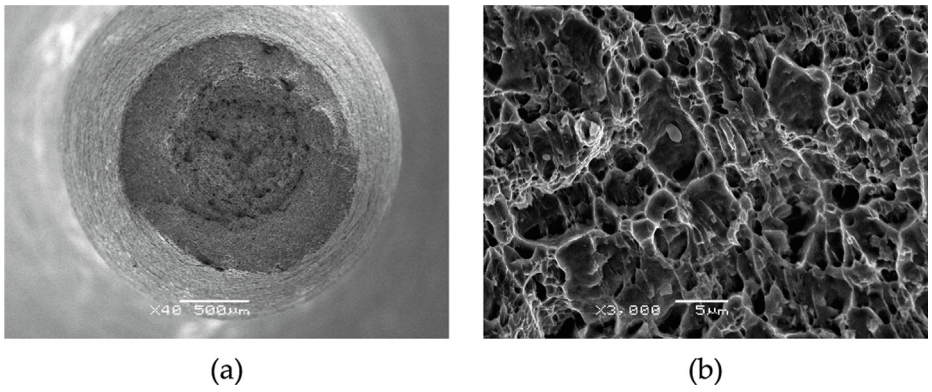

Fig. 19. SEM fractography of the uncorroded sample after 2.9 million cycles at 400 MPa.

equation (21). Corrosion results in entropy production and growth of TSI, which in turn accelerates the entropy production related to fatigue. These two phenomena are not completely independent in the model: existence of pre-corrosion accelerates the fatigue degradation through the TSI present in the last term of Eq. (21).

It is shown in Fig. 16 that the fatigue data of pre-corroded samples is much more scattered than uncorroded samples. This result is expected because of the defects and corrosion pits created in the sample's gauge section during corrosion. Also, chloride ions penetrate these defects randomly despite having the same NaCl concentration and the same corrosion time. In the microplasticity model, we use an average activated micro-defects ratio to account for the accelerated crack initiation process due to the stress concentration on these defects. Given the thermodynamic equation, the corrosion entropy production equation introduced in section 2 (the first two terms of equation (21)) depicts the amount of entropy generation for the formation of these defects. The TSI evolution due to pre-corrosion based on corrosion entropy production quantified the amount of damage/degradation to the sample in the corrosion process. And as mentioned, the growth of TSI during corrosion accelerates entropy production during fatigue. Finally, the fatigue life predicted by TSI in the Unified mechanics theory based on Boltzmann entropy formulation yields stochastic expected value. The scattered fatigue data of corroded samples due to the random distribution of surface defects and corrosion pits does not affect the results of UMT-predicted fatigue life. If more experimental fatigue

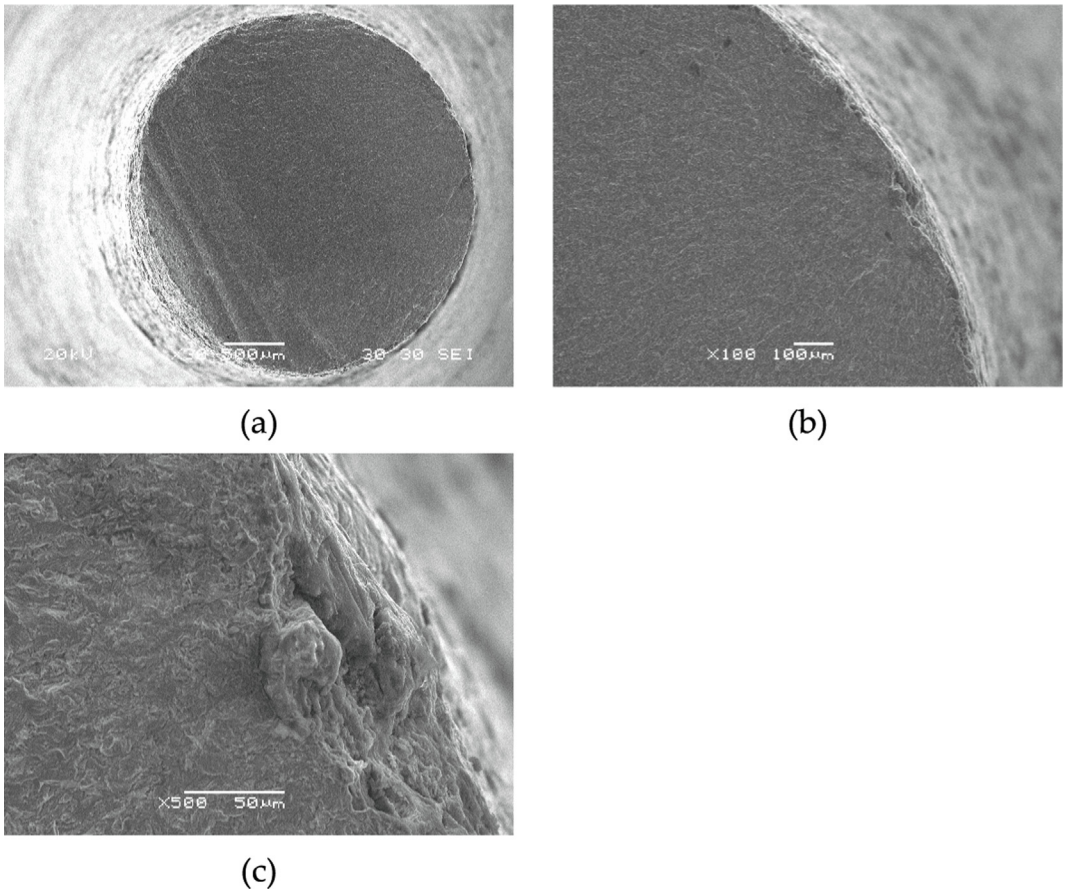

Fig. 20. SEM fractography of the pre-corroded sample after 7.2 million cycles at 370 MPa.

data are provided, we expect the experimental fatigue curve will be closer to the model simulations, which are based on Boltzmann distribution[1].

4.1. Calculation of entropy generation and evolution of TSI due to the kinetics of electrochemical activation overpotential

Estimating entropy generation due to electrochemical corrosion ΔS_{act} requires the calculation of equation (7). The electrochemical parameters vary according to the corrosion immersion time during the corrosion process. To estimate the entropy generation, three sets of data were used, based on the corrosion parameters obtained from the Tafel plots (Table 4 and Table 6).

Besides the above parameters, we have the following constants: surface area 1.614 cm^2, exchange current densities for metal oxidation and reduction of dissolved oxygen $j^0_{Fe} = 10^{-4}$ $10^{-5} A/cm^2$, $j^0_{O_2} = 10^{-6}$ $3 \times 10^{-7} A/cm^2$(described previously), and the number of electrons in the electrochemical reaction $z_M = 2$, $z_O = 1$.

Using the parameters given above ΔS_{act} can be computed. In the following, three sets of exchange current densities will be implemented in the model to estimate the corresponding entropy production, using a test overpotential of $\eta = 50mV$.

1. Lower bound: $j^0_{Fe} = 10^{-5} A/cm^2$, $j^0_{O_2} = 10^{-6} A/cm^2$
2. Middle range: $j^0_{Fe} = 5 \times 10^{-5} A/cm^2$, $j^0_{O_2} = 7 \times 10^{-7} A/cm^2$
3. Upper bound: $j^0_{Fe} = 10^{-4} A/cm^2$, $j^0_{O_2} = 3 \times 10^{-7} A/cm^2$

The reason for comparing different ranges of exchange current densities is that the exchange current density is related to the concentration of oxidized and reduced species, which we cannot directly measure from the test.

Fig. 22 shows the simulated cumulative entropy production and the TSI evolution for the electrochemical reaction when there exists an overpotential of + 50 mV. It shows that under the same applied overpotential, the higher the metal oxidation exchange current density, the more entropy is generated during the corrosion process. Therefore, the TSI value is larger for the higher oxidation exchange current density. The charge transfer coefficients are assumed to vary linearly within the 40 days range, based on the three sets of data given in Table 6.

However, during the 40-day corrosion immersion test, no external electrode overpotential was applied. In this case, the anodic flux for metal dissolution $J_{M,a}$ and the cathodic flux for the evolution of dissolved oxygen $J_{O,c}$ after conversion should be both equivalent to the corrosion current I_{corr}, according to Fig. 1. The driving force, in this special case, is the potential difference ΔE between the oxidized or reduced species. Therefore, the entropy generation is merely due to ΔE and I_{corr},

$$\begin{aligned}\Delta S_{act} &= \frac{1}{T}\int_{t_0}^{t} (J_{M,a}\Delta E + J_{O,c}\Delta E)dt_{corr} \\ &= \frac{1}{T}\int_{t_0}^{t} \left[I_{corr}(E^0_{H^2} - E^0_{Fe^{2+}}) + I_{corr}(E^0_{O_2} - E^0_{H^2})\right]dt_{corr} \\ &= \frac{1}{T}\int_{t_0}^{t} \left[I_{corr}(E^0_{O_2} - E^0_{Fe^{2+}})\right]dt_{corr} \end{aligned} \quad (22)$$

where $E^0_{H^2}$ is the standard hydrogen electrode which is set to 0 V. The standard cell overpotential E^0 for the dissolution of iron $Fe \leftrightarrow Fe^{2+} + 2e^-$ and the evolution of dissolved oxygen

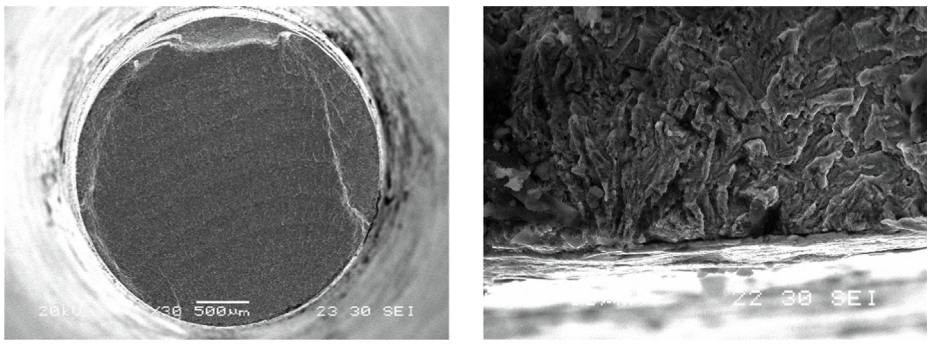

Fig. 21. SEM fractography of the uncorroded sample after 12.6 million cycles at 360 MPa.

Table 6
Charge transfer coefficients.

Time	0 days	20 days	40 days
$\alpha_{M.a}$	0.893	0.399	0.259
$\alpha_{O.C}$	0.075	0.748	0.747

$O_2 + 2H_2O + 4e^- \leftrightarrow 4OH^-$ are at − 0.440 V and + 0.401 V, respectively [54]. The corrosion current used here is a function of corrosion time, as shown in Fig. 12.

The simulated cumulative entropy production versus time is shown in Fig. 23. Since the corrosion current I_{corr} used in equation (22) is the mean value of the 16 test samples, a confidence level was built to illustrate the upper and lower bound of the simulation results.

4.2. Calculation of entropy generation due to chemical reaction overpotential

Typically, the contribution of chemical reaction overpotential is small compared to the activation overpotential mechanism if only a few chemical species interact in the corrosive environment. The calculation of entropy generation due to chemical reaction overpotential ΔS_{react} requires the determination of chemical reaction rate and chemical affinity, as described in equation (9).

In this study, entropy production due to corrosion focused only on the simple redox reaction (11). The number of chemical reactions involved r in this case is equivalent to 2. Therefore, we use the chemical reaction rate and chemical affinity of metal dissolution and dissolved oxygen evolution to estimate entropy production.

In equation (9), the chemical reaction affinity A_j can be estimated by $\tilde{A} = zF(E - E_{corr})$. On the other hand, calculating the reaction rate, υ_j, requires parameters such as rate constants k_a, k_c and the concentration of oxidized and reduced species C_O and C_R, respectively [15–17]. Since they cannot be measured directly during the corrosion test, we used the estimated corrosion rate as a first approximation. Table 7 shows the average corrosion rates of the test samples at different exposure periods.

Using the atomic mass of the iron (Fe) 55.85 g/mol, we can approximate the rate of metal dissolution $Fe \rightarrow Fe^{2+} + 2e^-$, to the same units as υ_j in equation (9) (mole/s). Owing to the electroneutrality requirement (i.e., all electrons produced in the anodic reaction must be consumed in the cathodic reaction), the oxidation and reduction reactions must occur simultaneously and at an equal rate [55].

Finally, the entropy generation due to corrosion reaction overpotential ΔS_{react} can be calculated, assuming that the reaction rate varies linearly according to Table 7. The simulated cumulative entropy production versus time is shown in Fig. 24. However, it

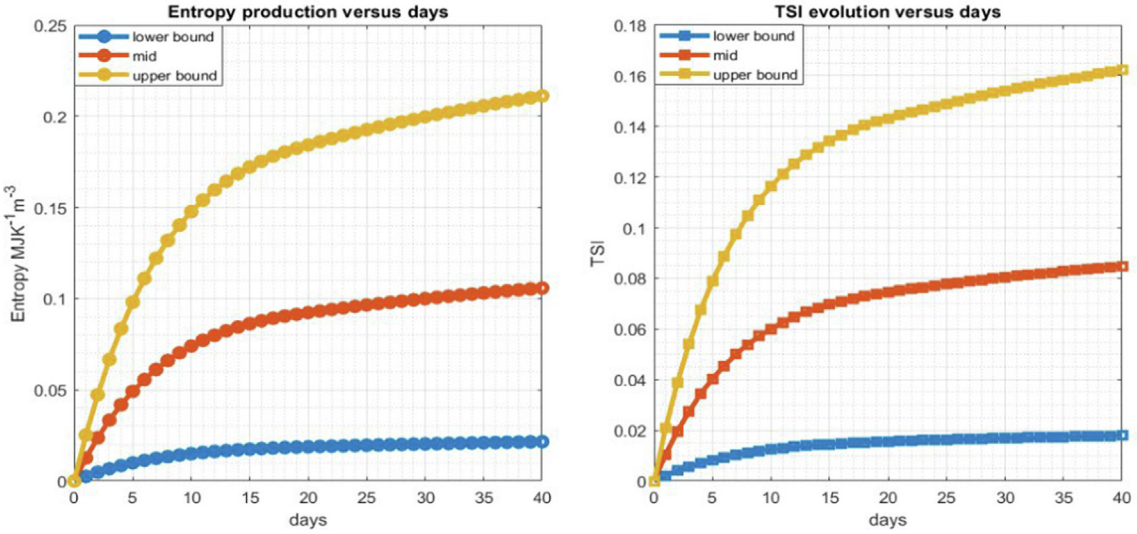

Fig. 22. Cumulative entropy production and TSI evolution as a function of corrosion time, due to corrosion.

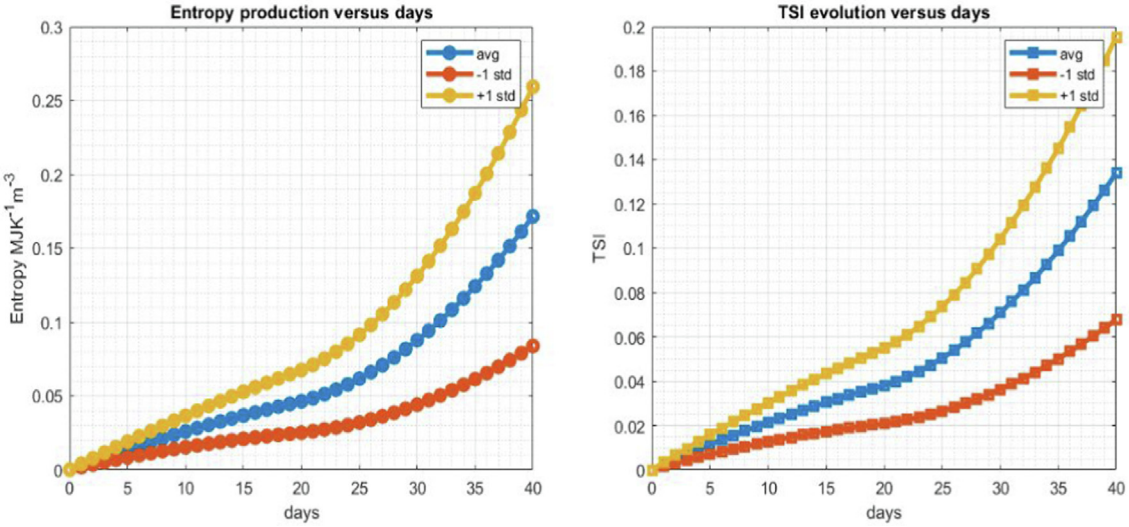

Fig. 23. Cumulative entropy production and TSI evolution versus days during the 40-day corrosion immersion test, due to the kinetics of electrochemical activation overpotential. The yellow line is the simulation with a + 1 standard deviation of the corrosion current, while the red line is the simulation with a −1 standard deviation of the corrosion current (for a confidence level of about 68 %). (For interpretation of the references to colour in this figure legend, the reader is referred to the web version of this article.)

is shown that the entropy production due to the chemical reaction overpotential is negligible compared to the activation overpotential mechanism. Fig. 25 shows the entropy generation and TSI evolution from the summation of these two mechanisms.

4.3. Calculation of entropy generation and evolution of TSI due to mechanical loading (ultrasonic vibration)

The entropy generation due to ultrasonic vibration has been extensively studied in [7]. Table 8 and Table 9 below summarize the material properties of the test samples.

Table 7
Corrosion rate for test samples in the form of mass loss.

Units/time	0 day	20 days	40 days
µpy	126.1700	88.2026	473.2154
g m^{-2} day^{-1}	0.069	0.048	0.26

Among the three entropy production mechanisms during ultrasonic vibration in equation (17), microplasticity is the most dominant. The amount of microplastic entropy production is sensitive to two parameters: (1) the volume fraction of activated micro-defects f_v, and (2) the microscopic yield stress σ_y^μ that determines the microplastic regime.

It should be emphasized here that the material properties in Table 8 are obtained from uncorroded samples. As observed from the SEM images, after corrosion the volume fraction of defects sites is increased due to the diffusion of chloride ions inside the samples. The microscopic yield stress (the fatigue limit) also decreased to 354 MPa, as shown in the SN curve of the corroded samples. Therefore, we choose to use a f_v value of 25 % and σ_y^μ of 354 MPa to calculate entropy production due to microplasticity.

Using the above parameters, the cumulative entropy generation of the specimen under mechanical loading is shown in Fig. 26. The TSI evolution of the specimen under mechanical loading is presented in Fig. 27. It should be emphasized that TSI evolution due

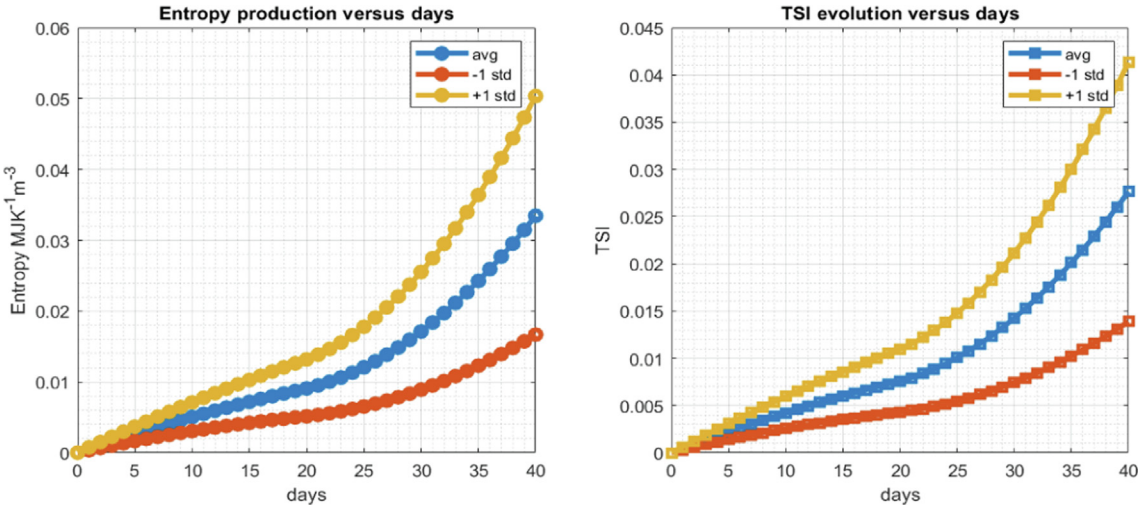

Fig. 24. Cumulative entropy production and TSI evolution versus days during the 40-day corrosion immersion test, due to chemical reaction overpotential. The yellow line is the simulation with a + 1 standard deviation of the corrosion rate, while the red line is the simulation with a −1 standard deviation of the corrosion rate. The confidence interval is around 68 %. (For interpretation of the references to colour in this figure legend, the reader is referred to the web version of this article.)

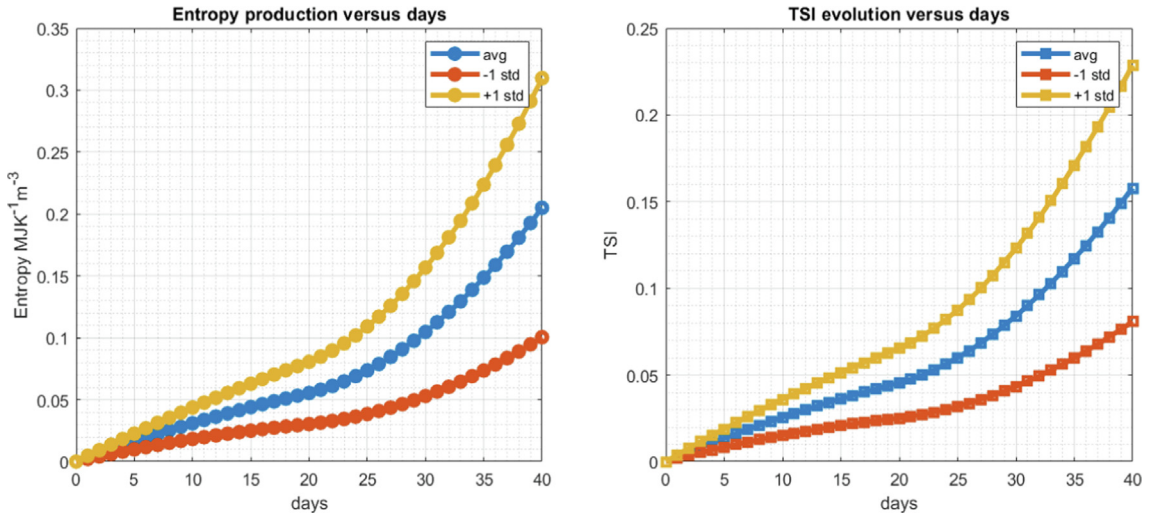

Fig. 25. Cumulative entropy production and TSI evolution versus days during the 40-day corrosion immersion test, due to both activation overpotential and chemical reaction overpotential.

Table 8
Material properties for USA A656 steel [7].

Young's modulus	197265 MPa	Macroscopic yield stress σ_y	400 MPa
Hardening coefficient	879 MPa	Microscopic yield stress σ_y^{μ}	368 ± 3.3 MPa
Poisson's ratio	0.27	Thermal expansion coefficient	$12.6{\cdot}10^{-6}$ K^{-1}
Density	7820 Kg m^{-3}	Specific heat capacity	470 J $Kg^{-1}K^{-1}$
The volume fraction of inclusions,f_v	20 %	Thermal conductivity,k_h	50W$K^{-1}m^{-1}$
Critical thermodynamic index	$\phi_{cr} = 0.97$	Frequency coefficient Ψ_f	$5{\cdot}10^{-3}$

Table 9
Parameters used in the proposed model in equation (19) [7].

Parameter	Symbol	Value	Units
Lattice constants	a	2.856	$10^{-10}m$
Magnitude of Burgers vector	b	60% of $0.87a$ 20% of $1.00a$ 20% of $1.41a$	Angstrom
Shear modulus	μ	7.76×10^4	MPa
Taylor's hardening parameter	α_H	1	–
Initial dislocation density	ϱ	0.88×10^{14}	m/m^3
Drag coefficient due to transverse phonon drag	B^{drag}	0.02	mPa · s
Dislocation density increment in each cycle	$\Delta\varrho$	1.523×10^{14}	m/m^3

to mechanical loading should start from the endpoint of the TSI value due to corrosion instead of 0. Because entropy is an additive property; therefore, the contribution from corrosion must be included.

The unified mechanics theory-based model simulation S—N curve for the uncorroded samples and corroded samples (40 days of corrosion time) are presented in Fig. 28, based on the evolution of TSI. It is shown that the corrosion degradation of the sample results in a decrease in fatigue life and fatigue limit. According to the simulation, when the stress amplitude is at 400 MPa, the fatigue life decreases from 2.79×10^6 to 1.58×10^6 cycles due to the corrosion degradation, which is around a 40 % reduction in fatigue life.

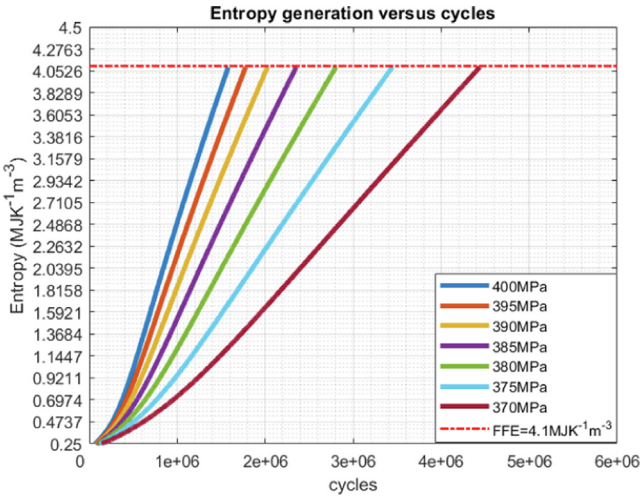

Fig. 26. Cumulative evolution production of the pre-corroded samples subjected to ultrasonic vibration continued from Fig. 25 (left). The cumulative entropy production continues from 0.25 $\frac{MJ}{Km^3}$.

Fig. 28 is used to validate the model. To show the corrosion time-dependent effect (i.e. the level of fatigue life reduction versus corrosion time) directly on the sN-curve, more fatigue tests would be needed. For example, a series of fatigue tests on corroded samples after 60 days of corrosion time and another series of fatigue tests on corroded samples after 80 days of corrosion time, etc. would be needed. At this moment, we are unable to provide this information due to the limited number of samples.

5. Conclusions

1. A fatigue life prediction model for pre-corroded metals based on the unified mechanics theory is presented. The entropy generation mechanism is divided into two categories: the entropy generation due to corrosion and the entropy generation due to mechanical dissipation. For corrosion, the dominant entropy generation mechanisms are (1) the kinetics of activation overpotential and (2) the chemical reaction overpotential. For

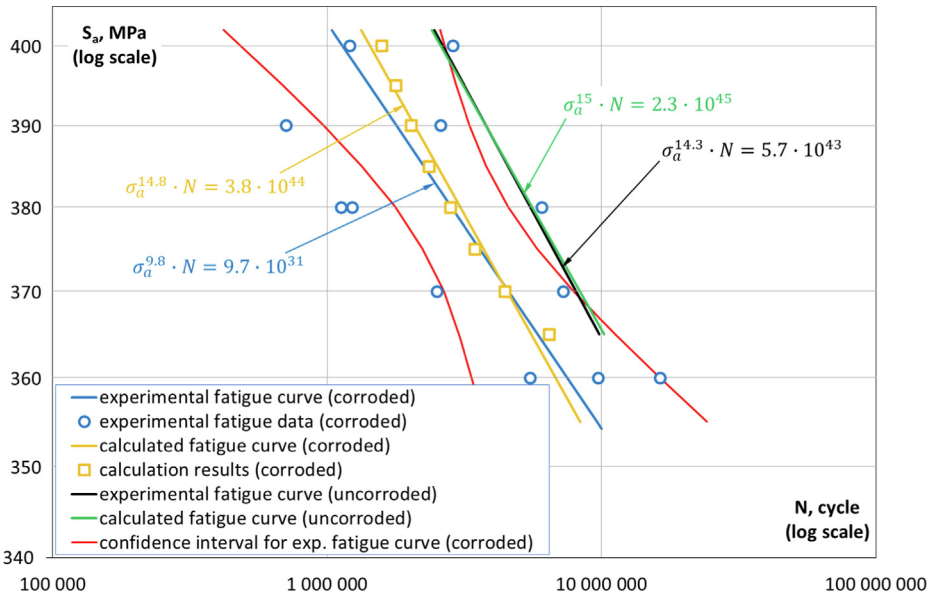

Fig. 28. Comparison of experimental data with model simulations of the S—N curve for the pre-corroded and uncorroded samples.

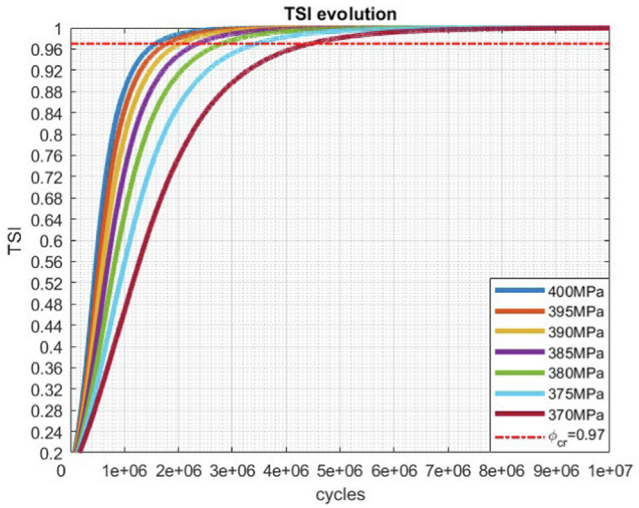

Fig. 27. TSI evolution of the corroded samples subjected to ultrasonic vibration continued from Fig. 25 (right). The TSI continued from 0.2.

mechanical loading, the dominant entropy generation mechanisms are (1) thermal conduction, (2) internal friction, and (3) microplasticity.

2. The electrochemistry of metal corrosion and the corresponding entropy generation mechanism is thoroughly studied. By obtaining the polarization parameters from the potentiostat polarization test, the entropy generation of the electrochemical corrosion with any applied overpotential is estimated. The detailed experimental procedure is presented. Experiment results are compared with other experiment results published in the literature.
3. When no external overpotential is applied, the entropy production can be estimated using the product of the potential difference and corrosion current. The entropy generation in the 40-day immersion is estimated, considering both activation overpotential and chemical reaction overpotential. Since some polarization parameters are mean values from 16 samples, the upper bound and lower bound of entropy production due to corrosion can be plotted using ± 1 standard deviation of the parameters. However, it does not affect the fatigue life of pre-corroded samples much because the entropy production during corrosion is one order of magnitude smaller than the entropy production during mechanical loading.
4. Finally, the fatigue life of pre-corroded samples is predicted by adding the cumulative entropy and TSI from the results of corrosion simulation with the cumulative entropy production and TSI evolution during ultrasonic vibration. The simulation results match the experimental data quite well in the region of low-stress amplitude. We believe that the deviation of the simulated data with respect to test data at higher stress amplitude is due to (1) the propagation of uneven corrosion-induced micro-defects at higher stress levels and (2) corrosion pitting that causes higher stress concentration, leading to higher microplasticity than the expected value at median stress levels. Additional entropy generation due to microplasticity at 400 MPa may be necessary. However, the main purpose of this study is to understand the very high cycle fatigue life of pre-corroded metals at stress levels well below the yield stress of the material.

Data availability

The raw/processed data required to reproduce these findings cannot be shared at this time as the data also forms part of an ongoing study.

Declaration of Competing Interest

The authors declare that they have no known competing financial interests or personal relationships that could have appeared to influence the work reported in this paper.

References

[1] C. Basaran, Introduction to Unified Mechanics Theory with Applications (1st ed.). Springer Nature: Berlin/Heidelberg, Germany, 2021;ISBN 978-3-030-57772-8.
[2] H.W. Lee, C. Basaran, A Review of Damage, Void Evolution, and Fatigue Life Prediction Models, Metals 11 (4) (2021) 609.
[3] C. Basaran, S. Nie, An Irreversible Thermodynamic Theory for Damage Mechanics of Solids, Int. J. Damage Mech 13 (3) (2004) 205–224.

[4] N. Bin Jamal M, A. Kumar, C. Lakshmana Rao, C. Basaran, Low Cycle Fatigue Life Prediction Using Unified Mechanics Theory in Ti-6Al-4V Alloys, Entropy 22 (1) (2019) 24.
[5] W. Egner, P. Sulich, S. Mroziński, H. Egner, Modelling thermo-mechanical cyclic behavior of P91 steel, Int. J. Plast 135 (2020), https://doi.org/10.1016/j.ijplas.2020.102820 102820.
[6] H.W. Lee, C. Basaran, Predicting High Cycle Fatigue Life with Unified Mechanics Theory, Mech. Mater. 164 (2022) 104116.
[7] H.W. Lee, C. Basaran, H. Egner, A. Lipski, M. Piotrowski, S. Mroziński, N. Bin Jamal M, C. Lakshmana Rao, Modeling ultrasonic vibration fatigue with unified mechanics theory, Int. J. Solids Struct. 236-237 (2022) 111313.
[8] N.B. Jamal M, C.L. Rao, C. Basaran, A unified mechanics theory-based model for temperature and strain rate dependent proportionality limit stress of mild steel, Mech. Mater. 155 (2021).
[9] W. Hu, Q. Shen, M. Zhang, Q. Meng, X. Zhang, Corrosion-Fatigue Life Prediction for 2024–T62 Aluminum Alloy Using Damage Mechanics-Based Approach, Int. J. Damage Mech 21 (8) (2011) 1245–1266, https://doi.org/10.1177/1056789511432791.
[10] G. Almaraz, R. Mora, Ultrasonic fatigue testing on high strength steel: Effect of stress concentration factors associated with corrosion pitting holes, Int. J. Damage Mech 22 (6) (2012) 860–877, https://doi.org/10.1177/1056789512468913.
[11] M. Liu, J. Xiong, C. Wang, A modified accumulation damage algorithm for predicting corrosion fatigue life by considering load interaction for aluminum alloys, Int. J. Damage Mech 28 (2) (2018) 270–290, https://doi.org/10.1177/1056789518763707.
[12] X. Yang, W. Fan, Z. Li, A continuum damage model for prediction of crack initiation life of pitting corrosion and fatigue, Int. J. Damage Mech 31 (6) (2022) 797–814.
[13] L. Onsager, Reciprocal Relations in Irreversible Processes, I. Physical Review 37 (4) (1931) 405–426, https://doi.org/10.1103/physrev.37.405.
[14] Gutman, E. (1998). Mechanochemistry of materials. Cambridge International Science Publishing.
[15] ChangHoon Lim and MZB (2014), Lecture 13: Butler-Volmer equation, Electrochemical Energy Systems, MIT OpenCourseWare.
[16] C. Page, Corrosion and protection of reinforcing steel in concrete, Durability Of Concrete And Cement Composites 136–186 (2007), https://doi.org/10.1533/9781845693398.136.
[17] B. Popov, Electrochemical Kinetics of Corrosion, Corros. Eng. 93–142 (2015), https://doi.org/10.1016/b978-0-444-62722-3.00003-3.
[18] J. Bockris, Z. Nagy, Symmetry factor and transfer coefficient. A source of confusion in electrode kinetics, J. Chem. Educ. 50 (12) (1973) 839, https://doi.org/10.1021/ed050p839.
[19] B. Lu, J. Luo, Synergism of Electrochemical and Mechanical Factors in Erosion−Corrosion, J. Phys. Chem. B 110 (9) (2006) 4217–4231, https://doi.org/10.1021/jp051985f.
[20] A. Imanian, M. Modarres, A Thermodynamic Entropy Approach to Reliability Assessment with Applications to Corrosion Fatigue, Entropy 17 (12) (2015) 6995–7020, https://doi.org/10.3390/e17106995.
[21] Y. Zou, J. Wang, Y. Zheng, Electrochemical techniques for determining corrosion rate of rusted steel in seawater, Corros. Sci. 53 (1) (2011) 208–216, https://doi.org/10.1016/j.corsci.2010.09.011.
[22] E. Salamci, S. Candan, F. Kabakci, Effect of microstructure on corrosion behavior of dual-phase steels, Met. Mater. 55 (02) (2017) 133–139, https://doi.org/10.4149/km_2017_2_133.
[23] H. Gerengi, N. Sen, I. Uygur, E. Kaya, Corrosion behavior of dual phase 600 and 800 steels in 3.5 wt.% NaCl environment, Journal Of Adhesion Science And Technology 34 (8) (2019) 903–915, https://doi.org/10.1080/01694243.2019.1688925.
[24] W. Osório, L. Peixoto, L. Garcia, A. Garcia, Electrochemical corrosion response of a low carbon heat treated steel in a NaCl solution, Materials And Corrosion 60 (10) (2009) 804–812, https://doi.org/10.1002/maco.200805181.
[25] Malina, J., Hadžipašić, A.B., & Nižník, Š. (2010). Electrochemical corrosion and hydrogen diffusivity in dual-phase steel.
[26] ASTM G102-89(2015)e1, Standard Practice for Calculation of Corrosion Rates and Related Information from Electrochemical Measurements, ASTM International, West Conshohocken, PA, 2015, www.astm.org.
[27] Kear, G. & Walsh, Frank. (2005). The characteristics of a true Tafel slope. Corros. Mater.. 30.
[28] L. Chen, J. Hu, X. Zhong, Q. Zhang, Y. Zheng, Z. Zhang, D. Zeng, Corrosion Behaviors of Q345R Steel at the Initial Stage in an Oxygen-Containing Aqueous Environment: Experiment and Modeling, Materials 11 (8) (2018) 1462, https://doi.org/10.3390/ma11081462.
[29] Trško, L., Nový, F., Bokůvka, O., & Jambor, M. (2018). Ultrasonic fatigue testing in the tension-compression mode. Journal of Visualized Experiments, (133). 10.3791/57007.
[30] S355J2 / 1.0577 – Steel Number - Chemical composition, equivalent, properties. Steelnumber.com. (2022). Retrieved 3 April 2022, from http://www.steelnumber.com/en/steel_composition_eu.php?name_id=10.
[31] ASTM A656/A656M-18(2018), Standard Specification for Hot-Rolled Structural Steel, High-Strength Low-Alloy Plate with Improved Formability, ASTM International, West Conshohocken, PA, 2018, www.astm.org.
[32] Reference 600+ Potentiostat/Galvanostat 5 MHz EIS Gamry Instruments. Gamry.com. (2022). Retrieved 4 April 2022, from https://www.gamry.com/potentiostats/reference-600-plus/.
[33] H. Parangusan, J. Bhadra, N. Al-Thani, A review of passivity breakdown on metal surfaces: influence of chloride- and sulfide-ion concentrations, temperature, and pH, Emergent Materials 4 (5) (2021) 1187–1203.
[34] H. Fakhri, K. Ragalwar, R. Ranade, On the use of Strain-Hardening Cementitious Composite covers to mitigate corrosion in reinforced concrete structures, Construction And Building Materials 224 (2019) 850–862, https://doi.org/10.1016/j.conbuildmat.2019.07.052.
[35] P. Refait, A. Grolleau, M. Jeannin, C. Rémazeilles, R. Sabot, Corrosion of Carbon Steel in Marine Environments: Role of the Corrosion Product Layer, Corrosion And Materials Degradation 1 (1) (2020) 198–218, https://doi.org/10.3390/cmd1010010.
[36] G. Eyu, G. Will, W. Dekkers, J. MacLeod, Effect of Dissolved Oxygen and Immersion Time on the Corrosion Behaviour of Mild Steel in Bicarbonate/Chloride Solution, Materials 9 (9) (2016) 748, https://doi.org/10.3390/ma9090748.
[37] Komalasari, Evelyn, I.D.R. Situmeang, D. Heltina, Cathodic protection on stuctures of carbon steel using sacrificial anode methode for corrosion control, IOP Conference Series: Materials Science And Engineering 845 (1) (2020), https://doi.org/10.1088/1757-899x/845/1/012015.
[38] H. Zhang, L. Yan, Y. Zhu, F. Ai, H. Li, Y. Li, Z. Jiang, The Effect of Immersion Corrosion Time on Electrochemical Corrosion Behavior and the Corrosion Mechanism of EH47 Ship Steel in Seawater, Metals 11 (8) (2021) 1317, https://doi.org/10.3390/met11081317.
[39] M. Roberts, A potentiostat for corrosion study, Br. J. Appl. Phys. 5 (10) (1954) 351–352, https://doi.org/10.1088/0508-3443/5/10/303.
[40] Bard, A., & Faulkner, L. (2000). Electrochemical methods and applications. Wiley-Interscience.
[41] Potentiostat/Galvanostat Electrochemical Instrument Basics. Gamry.com. (2021). Retrieved 13 July 2021, from https://www.gamry.com/application-notes/instrumentation/potentiostat-fundamentals/.
[42] Fakhri, H. (2019). Corrosion mitigation in reinforced concrete structures using engineered cementitious composites (Order No. 13886066). Available from Dissertations & Theses @ SUNY Buffalo; ProQuest Dissertations & Theses Global. (2305564873). Retrieved from https://www.proquest.com/dissertations-theses/corrosion-mitigation-reinforced-concrete/docview/2305564873/se-2?accountid=14169.
[43] M.C. Miller, M. (2022). RE-5 Electrode. Mcmiller.com. Retrieved 4 April 2022, from https://www.mcmiller.com/re-5-electrode-15108.
[44] H. Fakhri, K. Fishman, R. Ranade, A novel experimental method to determine the critical chloride content in cement-based composites, Construction And Building Materials 263 (2020), https://doi.org/10.1016/j.conbuildmat.2020.120101 120101.
[45] H. Fakhri, K. Fishman, R. Ranade, Rapid determination of critical chloride content in cement-based composites, Construction And Building Materials 268 (2021), https://doi.org/10.1016/j.conbuildmat.2020.121148 121148.
[46] ASTM G59-97(2020), Standard Test Method for Conducting 880 Potentiodynamic Polarization Resistance Measurements, ASTM 881 International, West Conshohocken, PA, 2020, www.astm.org.
[47] ASTM G61-86(2018), Standard test method for conducting cyclic 883 Potentiodynamic polarization measurements for localized corrosion 884 susceptibility of iron-, nickel-, or cobalt-based alloys, ASTM International, 885 West Conshohocken, PA, 2018.
[48] E. McCafferty, Validation of corrosion rates measured by the Tafel extrapolation method, Corros. Sci. 47 (12) (2005) 3202–3215, https://doi.org/10.1016/j.corsci.2005.05.046.
[49] M. Amin, K. Khaled, S. Fadl-Allah, Testing validity of the Tafel extrapolation method for monitoring corrosion of cold rolled steel in HCl solutions – Experimental and theoretical studies, Corros. Sci. 52 (1) (2010) 140–151, https://doi.org/10.1016/j.corsci.2009.08.055.
[50] M. Amin, K. Khaled, Q. Mohsen, H. Arida, A study of the inhibition of iron corrosion in HCl solutions by some amino acids, Corros. Sci. 52 (5) (2010) 1684–1695, https://doi.org/10.1016/j.corsci.2010.01.019.
[51] A. Choubey, R. Balasubramaniam, B. Basu, Effect of replacement of V by Nb and Fe on the electrochemical and corrosion behavior of Ti–6Al–4V in simulated physiological environment, Journal Of Alloys And Compounds 381 (1–2) (2004) 288–294, https://doi.org/10.1016/j.jallcom.2004.03.096.
[52] Jones, D. A. (1992). Principles and prevention of corrosion. New York: Macmillan Pub. Co.
[53] W. Tait, An introduction to electrochemical corrosion testing for practicing engineers and scientists, PairODocs (1994). Publications.
[54] W. Callister, D. Rethwisch, Materials science and engineering and introduction. John Wiley & Sons, Inc., 2007.
[55] S. Virtanen, Electrochemical Theory | Corrosion, Encyclopedia Electrochem. Power Sources 56–63 (2009), https://doi.org/10.1016/b978-044452745-5.00026-5.